batteries

MDPI

Article

A Comprehensive Model and Experimental Investigation of Venting Dynamics and Mass Loss in Lithium-Ion Batteries Under a Thermal Runaway

Ai Chen [1], Resul Sahin [1], Marco Ströbel [1,2], Thomas Kottke [3], Stefan Hecker [3] and Alexander Fill [1,2,*]

[1] Institute for Photovoltaics, University of Stuttgart, Pfaffenwaldring 47, 70569 Stuttgart, Germany; ai.chen@ipv.uni-stuttgart.de (A.C.); resul.sahin@ipv.uni-stuttgart.de (R.S.); marco.stroebel@ipv.uni-stuttgart.de (M.S.)
[2] MAP Battery Tests GmbH, Hauptstraße 117, 74599 Hengstfeld, Germany
[3] Rolls-Royce Power Systems, Maybachplatz 1, 88045 Friedrichshafen, Germany; thomas.kottke@ps.rolls-royce.com (T.K.); stefan.hecker@ps.rolls-royce.com (S.H.)
* Correspondence: alexander.fill@ipv.uni-stuttgart.de

Abstract: Thermal runaway (TR) has become a critical safety concern with the widespread use of lithium-ion batteries (LIBs) as an energy storage solution to meet the growing global energy demand. This issue has become a significant barrier to the expansion of LIB technologies. Addressing the urgent need for safer LIBs, this study developed a comprehensive model to simulate TR in cylindrical 18650 nickel cobalt manganese (NMC) LIBs. By incorporating experiments with LG®-INR18650-MJ1 cells, the model specifically aimed to accurately predict critical TR parameters, including temperature evolution, internal pressure changes, venting phases, and mass loss dynamics. The simulation closely correlated with experimental outcomes, particularly in replicating double venting mechanisms, gas generation, and the characteristics of mass loss observed during TR events. This study confirmed the feasibility of assuming proportional relationships between gas generation and the cell capacity and between the mass loss from solid particle ejection and the total mass loss, thereby simplifying the modeling of both gas generation and mass loss behaviors in LIBs under TR. Conclusively, the findings advanced the understanding of TR mechanisms in LIBs, providing a solid foundation for future research aimed at mitigating risks and promoting the safe integration of LIBs into sustainable energy solutions.

Keywords: lithium-ionbattery; thermal runaway; venting

check for updates

Academic Editor: Prodip K. Das

Received: 31 December 2024
Revised: 9 February 2025
Accepted: 21 February 2025
Published: 3 March 2025

Citation: Chen, A.; Sahin, R.; Ströbel, M.; Kottke, T.; Hecker, S.; Fill, A. A Comprehensive Model and Experimental Investigation of Venting Dynamics and Mass Loss in Lithium-Ion Batteries Under a Thermal Runaway. *Batteries* **2025**, *11*, 96. https://doi.org/10.3390/batteries11030096

Copyright: © 2025 by the authors. Licensee MDPI, Basel, Switzerland. This article is an open access article distributed under the terms and conditions of the Creative Commons Attribution (CC BY) license (https://creativecommons.org/licenses/by/4.0/).

1. Introduction

1.1. Motivation

In the new era of the highly developed society, the demand for energy has been increasing with the emergence of industrialization and the integration of information technology. A global shift towards more sustainable and environmentally friendly energy solutions is ongoing, particularly in the area of energy storage.

Lithium-ion batteries (LIBs) have appeared as a key technology to meet these demands due to their high energy density, efficiency, long cycle life, and environmental compatibility. They have already become the backbone of many electronic devices and are increasingly being used in electric vehicles (EVs) and grid-scale energy storage systems, contributing significantly to the reduction in greenhouse gas emissions. Despite their widespread adoption, LIBs have also brought safety issues such as thermal runaway (TR), which can lead to serious safety risks such as fires and explosions [1–6] .

Thermal runaway is a critical phenomenon where a battery cell undergoes an uncontrollable increase in temperature, triggering a cascade of exothermic reactions that rapidly liberate substantial energy in a short duration. This can result in a significant increase in temperature and pressure, which can lead to an explosion or fire [1–4,7–18]. During TR, the increase in the battery temperature not only causes electrolyte evaporation [19], but also triggers reactions that produce a large volume of gasses [20]. This combination can result in a sharp increase in the internal pressure, leading to the expansion of the battery casing.

The venting process is a critical safety feature designed to mitigate the pressure buildup within a battery cell during TR [19,21]. As the internal pressure reaches a critical threshold in a battery equipped with a safety vent valve, this valve opens, releasing a mixture of electrolyte vapors, reactive gasses, and solid particles into the surrounding environment [22]. In the absence of the vent valve, a feature often omitted in pouch cell designs, the mixture typically leaks and bursts from the sealant edges of the battery [21]. Together with the previous evaporation stage, this whole process consumes energy and partly cools the battery [19]. However, it often cannot stop the process of TR, where the cell temperature continues to rise steeply. The high temperature and substantial proportion of flammable gas in the resulting mixture often lead to a second venting eruption in the form of explosions and fires, appearing as jet flames [23]. The cell loses the most material during this process and shows a peak in its temperature. After consuming or losing the major mass of its active material, the TR reaches an end, where the battery is cooled by the ambient environment.

To optimize the cell and battery design in terms of safety and to gain further understanding, models are useful tools. Therefore, the accurate modeling of the venting process and mass loss is crucial for predicting the behavior of LIBs during TR and for developing strategies to lower the risks of causing a greater hazard.

1.2. Relevant Literature

Several studies have made significant contributions to the understanding and prediction of TR [2,7–18,24–28] and venting in LIBs [5,7,19,21,23,29–35]. There are research works providing comprehensive reviews of significant modeling works aimed at characterizing thermal runaway hazards and their triggering events in lithium-ion batteries, discussing the integration of battery aging effects, the interaction with testing, and the achievements and challenges in developing safer systems and fire prevention strategies using prediction tools [1,2]. To model TR in LIBs, researchers initially focused on uncovering the mechanism of TR by experimental studies and numerical modeling. Several works have concentrated on experimental and theoretical analyses to understand the TR process and its characteristics, providing valuable insights into the mechanisms, parameters, and conditions that influence TR events in LIBs [5,15,16,26,36]. In addition to the use of machine learning techniques combined with coupled electrical–thermal models [26], real-time monitoring now also contributes to the more precise identification of critical parameters for thermal runaway prediction [27,28]. By drawing parallels between TR processes and established combustion theories, these studies have revealed new insights into the mechanisms driving TR events, enhancing our understanding of the factors that govern TR behavior.

As for developing the TR model, Richard and Dahn [8,9] first investigated the thermal stability of lithium-ion cells, focusing on lithiated mesocarbon microbead (MCMB) material in various electrolytes under adiabatic conditions. Utilizing accelerated rate calorimetry (ARC), the study explored the effects of the lithium content, electrode surface area, electrolyte type, and initial heating temperature on the thermal stability of these materials. Based on the acquired data, the exothermic reaction kinetics of the solid electrolyte interphase (SEI) layer's decomposition and regeneration during TR in the negative electrode

have been characterized, leading to the development of a simple lumped model to predict TR events. Following that, Hatchard et al. [12] introduced a more comprehensive one-dimensional thermal model incorporating the TR reactions in the positive electrode, which was based on oven exposure testing and was used for assessing the effectiveness of cell designs in heat dissipation. Kim et al. [13] marked a significant advancement in TR modeling by moving beyond one-dimensional models to a comprehensive three-dimensional model and integrating electrolyte and binder decomposition. Their study offered detailed formulations for several potential exothermic reactions within the battery with geometrical features, enabling simulations that reveal how heat propagates through a cell during TR. These research efforts mainly focused on the heat generation and temperature change of the battery during the TR process, providing a primary understanding of the TR mechanisms. Building on these foundational studies, researchers have subsequently developed simplified and numerical models to predict and analyze the TR behavior of lithium-ion batteries [10,11,14,17,18,24,25].

With the deepened study of the TR process, more attention has been paid to more detailed failures from TR. During TR, the rising temperature of the battery not only causes the evaporation of the electrolyte [19] but also triggers reactions that produce a large volume of flammable or toxic gasses, which contributes to an increase in the internal pressure of the cell and can lead to combustion or explosion under higher temperatures. This mechanism has been extensively studied by experiments and quantification work by various researchers [20,29–32,36–38]. To first determine the composition of the main gasses generated from TR, Golubkov et al. [20] conducted a series of TR experiments on 18650 LIBs using various cathode materials, a combination of nickel manganese cobalt oxide (NMC) and lithium cobalt oxide (LCO), NMC, and lithium iron phosphate (LFP), and quantified the gasses with gas chromatography (GC) too. Subsequently, they further explored the TR characteristics of two commercially available types of 18650 LFP and lithium nickel cobalt aluminum oxide (NCA) cells and estimated the mass inventory based on the teardown results [37]. Shen et al. designed experiments using an adiabatic explosion chamber (AEC) under an inert atmosphere to test prismatic LIBs with LFP and different NMC cathode materials [38]. Besides the analysis of gas components, they also conducted a calculation of the flammability limit based on the generation of H_2 and thus evaluated the hazard degree of TR of LIBs with different cathodes. These experimental studies have clarified the types and quantities of gasses that can be generated during TR in specific types of LIBs, thereby enabling the advanced modeling of TR events.

Coman et al. first developed a lumped model for TR in 18650 LIBs, taking into account the evaporation of the electrolyte and the ejection of contents from the jelly roll [19]. They provided equations to describe the development of internal pressure and venting but also pointed out the difficulty of describing the mass loss directly with equations because of its unpredictability. Therefore, they estimated the mass loss rate based on statistical results from previous experiments. Mao et al. conducted experimental studies in both open environments and combustion chambers to investigate the combustion behavior of 18650 LIBs with NMC 532 cathodes. Their research focused on the correlation between the heat release, mass loss during TR, and the state of charge (SOC) of the LIBs [39]. Based on this and the estimation of the generated gas components from other experimental studies, they subsequently developed a lumped model to characterize the jet flow and fire dynamics of these LIBs under TR [23]. Similarly, Kong et al. developed a numerical model based on the assumption of gas generation to describe the venting dynamics and combustion behavior of 18650 LIBs with NCA cathodes. However, their model did not focus on solid particle ejection and mass loss [7]. Wang's team addressed this gap with their study by developing a multi-scale model for TR that integrates the ejection of solid particles and

mass loss [22]. They assumed that the mass loss from solid particle ejection is proportional to the total mass loss of the battery and conducted experiments in an open environment for venting flow analysis and in a sealed chamber to characterize the ejected particles.

The above literature review clearly indicates that the current trend in the field of TR modeling has shifted from detailing heat generation mechanisms to predicting TR behavior. While thermal behavior, such as the temperature change and heat release, remains the primary focus, there has been growing attention to venting and combustion behavior, including gas generation and release, particle ejection, venting flow dynamics, and the mass loss rate, in recent years. However, existing models often focus on isolated parameters, which limits their ability to accurately predict the overall TR behavior. To characterize and quantify the venting behavior of cylindrical LIBs and sodium-ion batteries (SIBs) during TR events, Fedoryshyna et al. developed a custom test bench equipped with shear force sensors and a high-speed camera to capture detailed data on venting dynamics, including the gas velocity, mass flow rate, and temperature variations [33]. They tested 21700 and 18650 LIBs with NMC811/SiC chemistry and 18650 SIBs with $NaMn_{1/3}Fe_{1/3}Ni_{1/3}O_2$/HC chemistry, all at a 100% SOC. TR was triggered through continuous heating, and measurements focused on the gas ejection velocity, recoil force, venting gas temperature, and mass loss during TR. Gillich et al. also developed a mechanical measurement approach to analyze the venting behavior during TR in 18650 LIBs [34]. Using a three-axis force sensor and high-frequency data logging, the setup enabled precise measurements of the recoil force and gas flow rates during TR in both high-power and high-energy 18650 cells.

Among these, predicting particle ejection and the mass loss rate poses the greatest difficulties due to the randomness of ejection and explosions, which also brings challenges to the reliability of the experiments for validation [35]. Therefore, the impact of the experiment setup on the TR and venting process has also become a study focus, including the triggering method for TR, the SOC, the cell format, etc. Willstrand et al. investigated how test setups, the SOC, and trigger methods influence the TR characteristics and gas release in large-format lithium-ion cells (157 Ah) [35]. They conducted 37 tests on large-format prismatic cells in both closed and open setups with six trigger methods, including heating, local heating, nail penetration, overcharge, and external fire, and with varied SOC levels. Their test results demonstrated a significant impact from various TR trigger methods and different SOC levels, particularly on the gas production rate, mass loss, and peak temperatures. They also noted that the trigger methods did not notably influence the total gas generation or gas composition, and the heating rate had a minimal effect on the TR onset temperature.

Given the evolving research trends in TR modeling, Table 1 presents a review of selected milestone studies that have significantly contributed to the modeling of TR and venting processes, highlighting their objectives and key researched parameters.

Table 1. Review on research of TR and venting.

Research	Goal	Research Object	Temperature/ Heat Profile	Gas Generation	Mass Loss	Venting Dynamics
Richard and Dahn [8,9]	1. Experimental study of the thermal stability of lithiated MCMB material in the electrolyte with an ARC test 2. Developing a simple lumped model for TR with the consideration of SEI reactions	MCMB electrode with $LiFP_6$ electrolyte	Yes	No	No	No
Hatchard et al. [12]	1. Developing a 1D model for TR with the consideration of reactions in the cathode 2. Experimental validation of the developed model with an ARC test	Format: 18650 Cathode: $LiCoO_2$	Yes	No	No	No
Kim et al. [13]	1. Developing a 3D model for TR integrating the electrolyte and binder decomposition 2. Studying the effect of the cell size on TR with the developed model	Format: cylindrical Cathode: $LiCoO_2$	Yes	No	No	No
Golubkov et al. [20,37]	1. Experimental studying of TR in LIBs with different cathodes (LCO, NMC, NCA, and LFP) in a sealed chamber 2. Quantifying the components of the generated gasses	Format: 18650 Cathode: $LiCoO_2$, $Li(Ni_{0.45}Mn_{0.45}Co_{0.1})O_2$, $LiFePO_4$, $Li(Ni_{0.8}Co_{0.15}Al_{0.05})O_2$	Yes	Yes [1]	No	No
Shen et al. [38]	1. Experimental analysis of the TR in LIBs with different NMC and LFP cathodes and their hazard potential with AEC tests 2. Quantifying the components of the generated gasses	Format: prismatic Cathode: $Li(Ni_{0.5}Mn_{0.3}Co_{0.2})O_2$, $Li(Ni_{0.6}Co_{0.2}Al_{0.2})O_2$, $Li(Ni_{0.8}Co_{0.1}Al_{0.1})O_2$, $Li(Ni_{0.9}Co_{0.05}Al_{0.05})O_2$, $LiFePO_4$	Yes	Yes [1]	No	No
Coman et al. [19]	Developing a lumped model for TR in 18650 LIBs with a focus on the venting of the electrolyte and the ejection of the contents from the jelly roll	Format: 18650 Cathode: $LiCoO_2$	Yes	Yes [2]	Yes	Yes
Mao et al. [39]	Experimental studying of the TR in 18650 LIBs in both an open environment and a combustion chamber to investigate the combustion behavior, mass loss, heat release, and the impact of the SOC on TR	Format: 18650 Cathode: $Li(Ni_{0.5}Mn_{0.3}Co_{0.2})O_2$	Yes	Yes [3]	Yes	No

Table 1. *Cont.*

Research	Goal	Research Object	Temperature/ Heat Profile	Gas Generation	Mass Loss	Venting Dynamics
Mao et al. [23]	1. Developing a lumped model to characterize the jet flow and fire dynamics of a 18650 LIB during TR, focusing on the gas generation, venting process, and flame behavior 2. Validating the model with an experiment in an open environment	Format: 18650 Cathode: $Li(Ni_{0.5}Mn_{0.3}Co_{0.2})O_2$	Yes	Yes [4]	No	Yes
Kong et al. [7]	1. Developing a numerical model to simulate the TR and jet fire of 18650 LIBs, focusing on the venting process and combustion of the vented gasses 2. Validating the model with an experiment in an open environment	Format: 18650 Cathode: $Li(Ni_{0.8}Co_{0.15}Al_{0.05})O_2$	Yes	Yes [4]	No	Yes
Wang et al. [22]	1. Developing a comprehensive multi-scale model that includes the multiphase process of particle venting during TR in LIBs 2. An experimental study of the TR in an open environment to analyze the venting flow and in a sealed chamber to characterize the ejected particles	Format: prismatic Cathode: $Li(Ni_xCo_yMn_z)O_2$ and $LiFePO_4$	Yes	Yes [4]	Yes	Yes
Fedoryshyna et al. [33]	Developing a custom test bench equipped with shear force sensors and a high-speed camera to capture detailed data on the venting dynamics	Format: 18650, 21700 Cathode: $Li(Ni_{0.8}Co_{0.1}Mn_{0.1})O_2$, $NaMn_{1/3}Fe_{1/3}Ni_{1/3}O_2$	Yes	Yes	Yes	Yes
Gillich et al. [34]	Developing a custom test bench applying the principles of momentum and mass conservation to analyze the dynamics of venting during TR	Format: 18650 Cathode: $Li(Ni_{0.8}Co_{0.1}Mn_{0.1})O_2$, $Li(Ni_{0.8}Co_{0.15}Al_{0.05})O_2$	Yes	Yes	Yes	Yes
Willstrand et al. [35]	Investigating how test setups, the SOC, and trigger methods influence the TR characteristics and gas release in large-format LIBs	Format: prismatic Cathode: $Li(Ni_{0.8}Co_{0.1}Mn_{0.1})O_2$	Yes	Yes	Yes	Yes

[1] Gas composition analysis with GC. [2] Just electrolyte vapor considered. [3] Just CO_x considered. [4] Assumption from other literature.

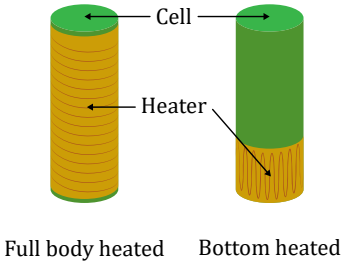
1.3. Contribution and Structure

This study presents a novel modeling approach to simulate the TR and venting process in LIBs, focusing on the accurate prediction of temperature development, gas generation, and mass loss. The model was validated by TR experiments using a type of high-energy 18650 cell (NMC811/SiC) in an open environment, triggered with heaters providing constant heating power, similar to the setup used in most of the referenced studies involving a venting process [7,19,23,39]. Our model successfully replicated the double venting mechanism observed in the experiments, which is a critical and often overlooked aspect of TR in LIBs. By incorporating the venting process and mass loss behavior, this study extends the understanding of the TR phenomenon, which aligns with the current research trends in this area, offering valuable insights and recommendations for future research to improve LIB safety and support the broader adoption of sustainable energy solutions.

The article is structured as follows: Section 2 presents the model approaches and experiment setup for validation. The simulation and experiment results will be demonstrated and discussed in Section 3. A conclusion will then be given in Section 4.

2. Methodology

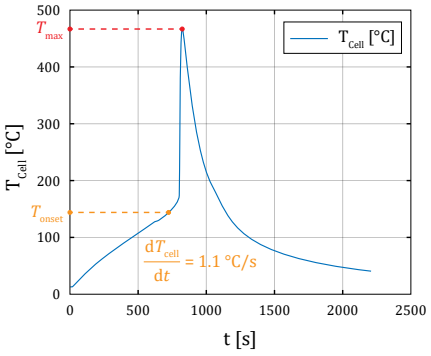
In this study, a novel modeling approach was developed to simulate the TR and venting process in LIBs, focusing on the temperature development, gas generation, and mass loss. Experiments using a type of high-energy 18650 cell, LG®-INR18650-MJ1, were conducted to parameterize and validate the model. An overview of the setup conditions and methodology of this study is shown in Figure 1, which includes a schematic illustration representing the two different heating methods adopted in our experiments, the number of experiments conducted under different heating conditions, and an example to demonstrate the onset temperature—the point after which the cell temperature increases uncontrollably—and the peak temperature. All measurements described in this study were conducted at MAP Battery Tests GmbH facilities.



(a)

heating method	Number of experiments for temperature	Number of experiments for mass loss fraction
20W full body	7	4
30W full body	4	3
50W bottom	2	1
70W bottom	3	3
90W bottom	3	3

(b)



(c)

Figure 1. An overview of the setup conditions and methodology of this study, with (**a**) a schematic illustration of cells with wire heaters glued to the full body area and just the bottom area, representing the two heating methods adopted in our experiments, (**b**) the number of experiments conducted under different heating conditions, and (**c**) an example to demonstrate the onset temperature, the inflection point of the slope of the temperature changing rate, and the peak temperature.

2.1. Model Approach

Given the complexity of the thermal reactions and venting dynamics during TR, advanced modeling approaches were implemented in MATLAB® (Version 2024b) to simulate the behavior of an LIB under TR. A flow chart of the modeling work performed in this research is shown in Figure 2 with the main inputs and outputs. The model developed

in this study comprises three distinct sub-models: the **(I)** 'Thermal Runaway Sub-model', **(II)** 'Internal Pressure Sub-model', and **(III)** 'Venting Sub-model'. Each sub-model has a specific focus and their outputs serve as inputs for the others, establishing an interconnected framework. These outputs are continually compared with the experimental results to validate and refine the model, ensuring that the final outputs are satisfactorily aligned with the observed data.

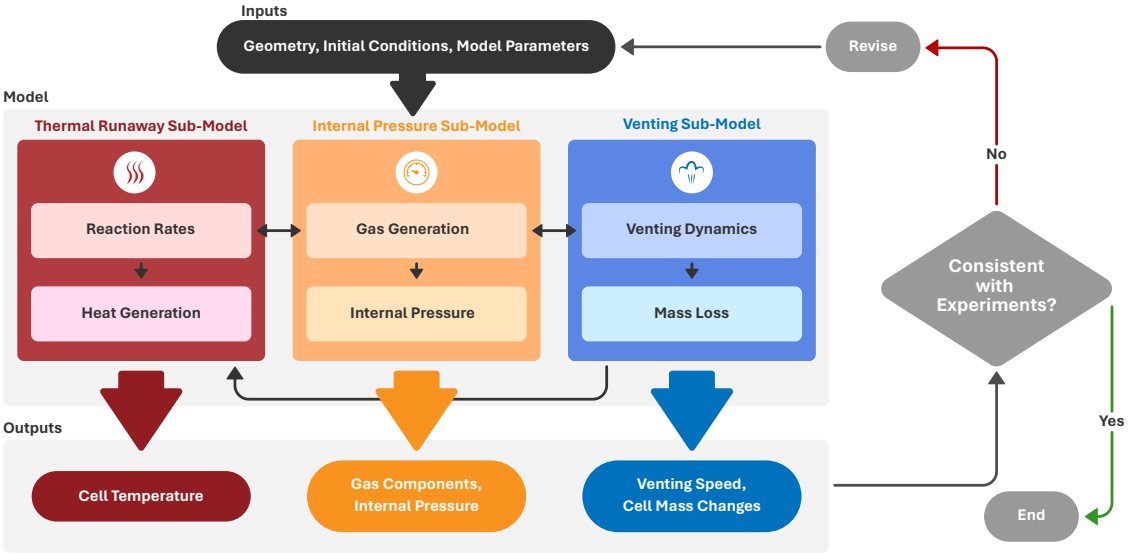


Figure 2. Flow chart of the model approach used, with the three sub-models and the main inputs and outputs.

2.1.1. Thermal Runaway Sub-Model

A flow chart of the TR sub-model is shown in Figure 3. The initiation of TR typically results from heat generated by reactions triggered at both the anode and cathode and in the electrolyte, which can be differentiated into separate reactions for discussion. In this work, an LIB with an NMC cathode was chosen to be modeled. Based on the findings of Richard and Dahn and Kriston et al. [8,9,40], we assumed the following reactions for the used cell type in the anode: SEI decomposition (A1), SEI regeneration (A2), a Li–electrolyte reaction (A3), and anode binder decomposition (A4). Meanwhile, in the cathode and electrolyte, the reactions were the autocatalytic decomposition of NMC (C1), electrolyte reactions (C2), NMC binder decomposition (C3), and the further decomposition of NMC with oxygen reactions (C4).

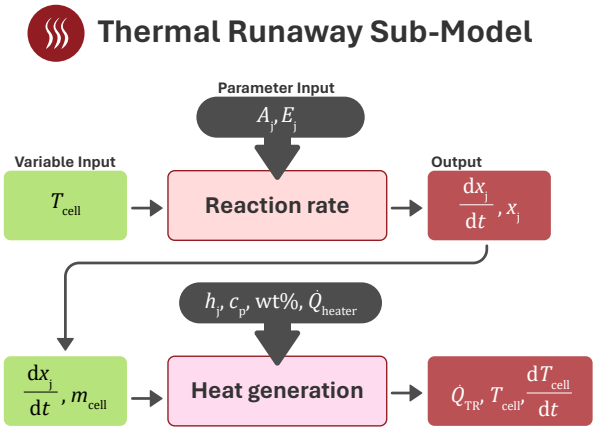


Figure 3. A flow chart of the thermal runaway sub-model.

A1—SEI Decomposition

When the temperature of a lithium-ion cell reaches around 90 °C, the SEI layer formed on the surface of the anode can decompose and release heat, which can contribute to triggering other reactions. This reaction has been modeled and validated by Richard et al. [8] through the following Arrhenius equations, Equations (1) and (2):

$$\frac{\mathrm{d}x_{\mathrm{SEId}}}{\mathrm{d}t} = -A_{\mathrm{SEId}} x_{\mathrm{SEId}}^{0.5} \exp\left(-\frac{E_{\mathrm{SEId}}}{\mathrm{RT}}\right) \tag{1}$$

$$\dot{Q}_{\mathrm{SEId}} = m_{\mathrm{an}} h_{\mathrm{SEId}} \left(-\frac{\mathrm{d}x_{\mathrm{SEId}}}{\mathrm{d}t}\right) \tag{2}$$

Equation (1) shows the rate of decomposition of the metastable part of the SEI layer as a function of time, $\mathrm{d}x_{\mathrm{SEId}}/\mathrm{d}t$, which depends on the frequency factor A_{SEId}, the activation energy E_{SEId}, and the temperature T. Equation (2) relates the amount of heat released during the SEI decomposition, Q_{SEId}, to the mass of the anode material m_{an}, the heat of the reaction h_{SEId}, and the rate of decomposition $\mathrm{d}x_{\mathrm{f}}/\mathrm{d}t$, which is negative due to the decreasing amount of the metastable SEI. Before decomposition, the initial mole fraction of the metastable part of the SEI layer is $x_{\mathrm{f0}} = 0.1$ [8]. The gas constant R was set to 8.314 $\mathrm{Jmol^{-1}K^{-1}}$ in the calculations.

A2—SEI Regeneration

The SEI regeneration process occurs after the decomposition of the SEI layer, with a peak at around 200 °C. During this process, intercalated lithium reacts with the electrolyte and deposits on the degenerated SEI film, resulting in the regeneration of a new film, which was modeled using Arrhenius-type equations as follows [8]:

$$\frac{\mathrm{d}x_{\mathrm{SEIr}}}{\mathrm{d}t} = -A_{\mathrm{SEIr}} x_{\mathrm{SEIr}} \exp\left(-\frac{z_{\mathrm{i}}}{z_0}\right) \exp\left(-\frac{E_{\mathrm{SEIr}}}{\mathrm{RT}}\right) \tag{3}$$

$$\frac{\mathrm{d}z_{\mathrm{i}}}{\mathrm{d}t} = A_{\mathrm{SEIr}} x_{\mathrm{SEIr}} \exp\left(-\frac{z_{\mathrm{i}}}{z_0}\right) \exp\left(-\frac{E_{\mathrm{SEIr}}}{\mathrm{RT}}\right) \tag{4}$$

$$\dot{Q}_{\mathrm{SEIr}} = m_{\mathrm{an}} h_{\mathrm{SEIr}} \left(-\frac{\mathrm{d}x_{\mathrm{SEIr}}}{\mathrm{d}t}\right) \tag{5}$$

Here, the rate of change of the intercalated lithium amount x_{SEIr} is related to the amount of lithium in the SEI layer per unit surface area, z_{i}, which can be used to present the thickness of the SEI diffusion layer. Given that the growth of the thickness of the SEI layer impacts the transport of lithium through this layer and consequently affects the rate of consumption of intercalated Li, a factor of $\exp(-z_{\mathrm{i}}/z_0)$ is incorporated. This factor serves to decrease the consumption rate of intercalated Li as the SEI layer expands. The variable z_0 represents the initial amount of Li in the SEI per unit surface area, with a value of 0.15 $\mathrm{m^{-2}}$. The heat generated during the SEI regeneration process is modeled by Equation (5) using the heat of the reaction h_{SEIr} [8].

A3—Li–Electrolyte Reaction

As the TR progresses further, a Li–electrolyte reaction takes place at elevated temperatures, even before the completion of A2. During this reaction, the regenerated SEI decomposes, and lithium directly reacts with the electrolyte. This process is faster and more energetic than A2, consuming the intercalated lithium in the anode and generating

hydrocarbons. Based on the specific electrolytes used, these subsequent reactions may happen [40]:

$$2\mathrm{Li} + \mathrm{C_3H_4O_3\ (EC)} \rightarrow \mathrm{Li_2CO_3} + \mathrm{C_2H_4}$$

$$2\mathrm{Li} + \mathrm{C_3H_6O_3\ (DMC)} \rightarrow \mathrm{Li_2CO_3} + \mathrm{C_2H_6}$$

$$2\mathrm{Li} + \mathrm{C_5H_{10}O_3\ (DEC)} \rightarrow \mathrm{Li_2CO_3} + \mathrm{C_4H_{10}}$$

As A3 begins before A2 is finished, both reactions consume intercalated lithium simultaneously, indicating that A2 and A3 should be coupled according to Kriston et al. [40], whose experiment showed an abrupt high heat flow during the process of A2. We fitted this coupled model represented by the following equation, where the frequency factor A_{LiE} and activation energy E_{LiE} are used:

$$\frac{\mathrm{d}x_{\mathrm{SEIr}}}{\mathrm{d}t} = -A_{\mathrm{SEIr}} x_{\mathrm{SEIr}} \exp\left(-\frac{z_{\mathrm{i}}}{z_0}\right) \exp\left(-\frac{E_{\mathrm{SEIr}}}{\mathrm{RT}}\right) - A_{\mathrm{LiE}} x_{\mathrm{SEIr}} \exp\left(-\frac{E_{\mathrm{LiE}}}{\mathrm{RT}}\right) \tag{6}$$

The generated heat can still be calculated using Equation (5), for the value of h_{SEIr} used in this work already includes the A3 reaction.

A4—Anode Binder Decomposition

Similarly, an Arrhenius-type single-component decomposition is proposed as an approximation to represent anode binder decomposition, with x_{AnB} being the dimensionless concentration of the binder and other components from the previous decomposition process, and A_{AnB}, E_{AnB}, and h_{AnB} being the thermal triplets for calculations [40]:

$$\frac{\mathrm{d}x_{\mathrm{AnB}}}{\mathrm{d}t} = -A_{\mathrm{AnB}} x_{\mathrm{AnB}} \exp\left(-\frac{E_{\mathrm{AnB}}}{\mathrm{RT}}\right) \tag{7}$$

$$\dot{Q}_{\mathrm{AnB}} = m_{\mathrm{an}} h_{\mathrm{AnB}} \left(-\frac{\mathrm{d}x_{\mathrm{AnB}}}{\mathrm{d}t}\right) \tag{8}$$

C1—Autocatalytic Decomposition of NMC

During the process of TR, the NMC material undergoes a self-accelerating decomposition process at over 200 °C [12,41]. It is typical for all models to consider only one decomposition reaction and describe it through an Arrhenius-type equation [40,42]:

$$\frac{\mathrm{d}x_{\mathrm{NMCd}}}{\mathrm{d}t} = -A_{\mathrm{NMCd}} x_{\mathrm{NMCd}} \exp\left(-\frac{E_{\mathrm{NMCd}}}{\mathrm{RT}}\right) \tag{9}$$

$$\dot{Q}_{\mathrm{NMCd}} = m_{\mathrm{ca}} h_{\mathrm{NMCd}} \left(-\frac{dx_{\mathrm{NMCd}}}{dt}\right) \tag{10}$$

C2—Electrolyte Reactions

As the temperature increases, the electrolyte evaporates at low temperatures, initially as an endothermic reaction. Subsequently, the remaining electrolyte undergoes decomposition. Under specific temperatures and mixing conditions with the released oxygen, there is also a possibility of the combustion of the electrolyte.

The generation of oxygen can be modeled using an Arrhenius-type equation summarized by Kristion et al. [40]:

$$\frac{\mathrm{d}x_{\mathrm{O2}}}{\mathrm{d}t} = -y_{\mathrm{O2}} A_{\mathrm{NMCd}} x_{\mathrm{NMCd}} \exp\left(-\frac{E_{\mathrm{NMCd}}}{\mathrm{RT}}\right), \tag{11}$$

which is highly related to the decomposition of NMC in C1. The factor y_{O2} is the stoichiometric amount of oxygen released with a value range from 0 to 1, which was chosen to be 0.1 in this work according to Kriston et al. [40].

Based on that, the consumption of the electrolyte through decomposition, evaporation, and combustion is coupled and modeled with the respective frequency factors A and activation energies E using Equations (12) and (13), while the generated heat is calculated with the heat of each reaction h and the mass of the electrolyte m_{El} using Equation (14):

$$\frac{dx_{EL}}{dt} = \frac{dx_{EL,eva}}{dt} + \frac{dx_{EL,dec}}{dt} + \frac{dx_{EL,com}}{dt} \tag{12}$$

$$\frac{dx_{EL}}{dt} = -A_{eva}x_{El}\exp\left(-\frac{E_{eva}}{RT}\right) - A_{dec}x_{El}\exp\left(-\frac{E_{dec}}{RT}\right) - A_{com}x_{El}x_{O2}\exp\left(-\frac{E_{com}}{RT}\right) \tag{13}$$

$$\begin{aligned}\dot{Q}_{El} = {} & m_{El}\cdot(-A_{eva}x_{El}\exp\left(-\frac{E_{eva}}{RT}\right)\cdot h_{eva} \\ & - A_{dec}x_{El}\exp\left(-\frac{E_{dec}}{RT}\right)\cdot h_{dec} - A_{com}x_{El}x_{O2}\exp\left(-\frac{E_{com}}{RT}\right)\cdot h_{com})\end{aligned} \tag{14}$$

Among these reactions, electrolyte combustion is influenced not only by the oxygen release but also by the mixing ratio of the electrolyte and oxygen, as well as the corresponding ignition point. Due to this complexity, not all studies have accounted for electrolyte combustion [3]. In light of these challenges, electrolyte combustion was not considered in our modeling work, allowing for more accurate results.

C3—NMC Binder Decomposition

Based on the work of Kriston et al. [40], the NMC cathode binder material was also determined to decompose during the TR process in the temperature range of 400–500 °C, which can be presented through equations with the thermal triplets for this reaction, A_{CaB}, E_{CaB}, and h_{CaB}:

$$\frac{dx_{CaB}}{dt} = -A_{CaB}x_{CaB}\exp\left(-\frac{E_{CaB}}{RT}\right) \tag{15}$$

$$\dot{Q}_{CaB} = m_{ca}h_{CaB}\left(-\frac{dx_{CaB}}{dt}\right) \tag{16}$$

C4—Further Decomposition of NMC with Oxygen Reactions

In the temperature range of 500–600 °C, the released oxygen burns the carbon or other organic compounds, triggering the further decomposition of the NMC material [40]. The mechanism is similar to that of the C1 reaction and can also be modeled similarly:

$$\frac{dx_{NMCf}}{dt} = -A_{NMCf}x_{NMCf}\exp\left(-\frac{E_{NMCf}}{RT}\right) \tag{17}$$

$$\dot{Q}_{NMCf} = m_{ca}h_{NMCf}\left(-\frac{dx_{NMCf}}{dt}\right) \tag{18}$$

Although oxygen release occurs during this process, the associated heat generation is incorporated into the terms h_{CaB} and h_{NMCf} in Equations (16) and (18). Therefore, it is not calculated separately in order to reduce the computational time and maintain the stability of the model.

Temperature Rise

In our modeling approach, the cells are considered both thermally and chemically lumped, meaning that the temperature within a single cell is assumed to be uniform. To

align with our experimental setup, the TR of the cell is triggered by an external heater with a fixed heating power until the cell reaches a specified temperature, T_{set}. Consequently, the temperature increase rate of the cell due to the external heater can be expressed as

$$\left.\frac{dT}{dt}\right|_{cell} = \frac{\dot{Q}_{heater}}{c_{p,cell} \cdot m_{cell}} \tag{19}$$

The heat generated from the TR reactions is another factor contributing to the temperature rise. Since the heat generation of each reaction has already been discussed above, the heat flow from thermal runaway can be determined by summing the heat contributions from each reaction, i, from A1 to A4 and C1 to C4:

$$\dot{Q}_{TR} = \sum \dot{Q}_i = \dot{Q}_{SEIr} + \dot{Q}_{SEId} + \dot{Q}_{AnB} + \dot{Q}_{NMCd} + \dot{Q}_{El} + \dot{Q}_{CaB} + \dot{Q}_{NMCf} \tag{20}$$

Therefore, considering the contribution of both the external heater and internal reactions, the temperature rise of the cell can be calculated as

$$\frac{dT}{dt} = \begin{cases} \frac{\dot{Q}_{heater} + \dot{Q}_{TR}}{c_{p,cell} \cdot m_{cell}}, & T \leq T_{set} \\ \frac{\dot{Q}_{TR}}{c_{p,cell} \cdot m_{cell}}, & T > T_{set} \end{cases} \tag{21}$$

2.1.2. Internal Pressure Sub-Model

A large volume of gas production is also observed during the TR process, originating from the electrolyte evaporation [19] and the TR reactions described in the thermal runaway sub-model [20,40]. This results in a sharp increase in the internal pressure of the cell. In our work, the modeled cell is a 18650 type, equipped with a safety valve. When the internal pressure reaches a critical threshold, the safety valve opens, releasing a mixture of electrolyte vapors, reactive gasses, and solid particles, thereby reducing the internal pressure [22,43]. This process is modeled with an internal pressure sub-model, with its workflow illustrated in Figure 4.

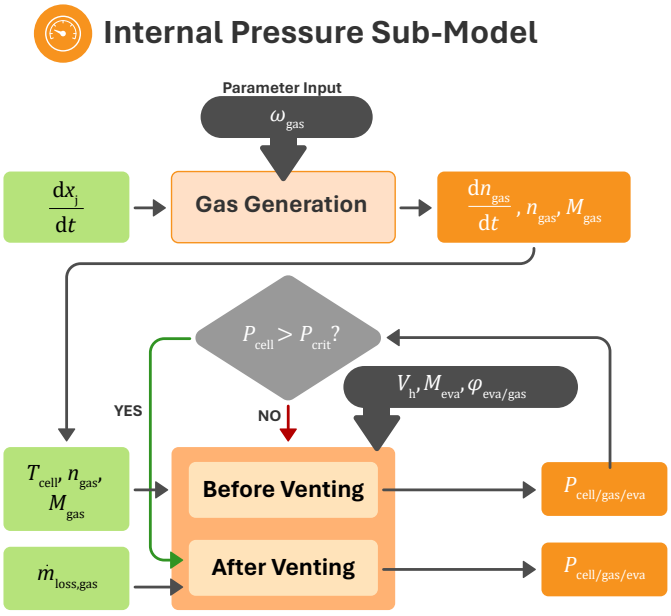


Figure 4. A flow chart of the internal pressure sub-model.

Gas Generation

As the temperature increases during TR with ongoing exothermic reactions, a significant amount of flammable or toxic gasses can be generated as products of the TR reactions

or side reactions, contributing to the increase in the internal pressure of the cell. This mechanism has been extensively studied through experiments and quantification work by various researchers [20,36–38]. Generally, the generation of these 6 types of gasses is focused on and studied: CO_2, CO, H_2, CH_4, C_2H_4, and C_2H_6 [44]. The reaction mechanism within the cell is complex and filled with uncertainty. Consequently, it is reasonable to simplify the modeling by assuming that the generation of each gas during a particular reaction stage corresponds to a single primary chemical reaction. This approach facilitates the clearer modeling of the relationship between gas generation and the reaction extent [22]. The CO_2 comes mainly from the decomposition of the SEI layer (A1), the reaction between the exposed lithium and electrolyte (A3), and the decomposition of the electrolyte (C2) [20,40]. Hydrogen, H_2, is produced primarily from the decomposition of the binder material, specifically polyvinylidene fluoride (PVDF) [20]. Besides CO_2, the generation of CO, CH_4, C_2H_4, and C_2H_6 can also be observed from the Li–electrolyte reaction (A3) [20,40]. The above-mentioned reaction mechanisms and their associated chemical equations are summarized in Table 2.

Table 2. The gas generation mechanisms.

TR Reactions	Gas Generation Mechanisms	Refs.
SEI decomposition	$(CH_2OCO_2Li)_2 \xrightarrow{\triangle} Li_2CO_3 + C_2H_4 + CO_2 + 0.5O_2$	[20]
Li–electrolyte reaction	$2Li^+ + C_3H_6O_3(DMC) + 2e^- \rightarrow CO + 2CH_3OLi$	[22,40]
	$Li^+ + C_3H_6O_3(DMC) + e^- + 0.5H_2 \rightarrow CH_4 + CH_3OCO_2Li$	
	$2Li + C_3H_6O_3(DMC) \rightarrow C_2H_6 + Li_2CO_3$	
PVDF binder decomposition	-CH2-CF2- + Li $\xrightarrow{\Delta H}$ LiF + -CH=CF- + $\frac{1}{2}H_2$	[20]
CMC + Li	CMC-OH + $Li^+ + e^- \rightarrow$ CMC-$Oli_{(s)} + 1/2\ H_{2(g)}$	[40]
Electrolyte decomposition	$C_3H_6O_3(DMC) + 3O_2 \rightarrow 3CO_2 + 3H_2O$	[22]

With the gas generation mechanisms established, the matrix $\omega_{a,b}$ shown in Equation (22) can be employed to quantitatively assess the contributions of each TR reaction to the production of specific gas components:

$$\begin{pmatrix} \Delta x_{A1} \\ \Delta x_{A3} \\ \Delta x_{A4} \\ \Delta x_{C2} \\ \Delta x_{C3} \end{pmatrix}^T \begin{pmatrix} \omega_{CO_2,1} & 0 & 0 & 0 & 0 & 0 \\ \omega_{CO_2,2} & \omega_{CO} & 0 & \omega_{CH_4} & \omega_{C_2H_4} & \omega_{C_2H_6} \\ 0 & 0 & \omega_{H_2,1} & 0 & 0 & 0 \\ \omega_{CO_2,3} & 0 & 0 & 0 & 0 & 0 \\ 0 & 0 & \omega_{H_2,2} & 0 & 0 & 0 \end{pmatrix} = (\Delta n_{CO_2}, \Delta n_{CO}, \Delta n_{H_2}, \Delta n_{CH_4}, \Delta n_{C_2H_4}, \Delta n_{C_2H_6}) \quad (22)$$

In this matrix, rows (1)–(5) correspond to the TR reactions discussed, while columns (1)–(6) represent the gas components CO_2, CO, H_2, CH_4, C_2H_4, and C_2H_6. The amount of gas b produced in reaction a is quantified using the coefficients ω_{ab}. Therefore, the amount of gas b produced over a specific time period, Δn_b, can be calculated using the formula provided in Equation (23):

$$\Delta n_b = \sum_{a=1}^{5} \omega_{ab} \Delta x_a \quad (23)$$

Golubklov et al., Shi et al., Shen et al., and Willstrand et al. have all conducted experiments on NMC LIBs [20,35,36,38]. The total amount of the gasses produced in their studies correlated well with the capacity of the LIBs, and their results with 100% SOC LIBs are detailed in Table 3.

Table 3. The gas generation results from the literature.

LIB Shape	Cathode	Capacity [Ah]	Gas Amount [mol]	Amount/Capacity [mol/Ah]	Ref.
18650	NMC4.5 4.5 1	1.5	0.15	0.100	[20]
Prismatic	NMC9 0.5 0.5	211	18.35	0.087	[36]
Prismatic	NMC9 0.5 0.5	256	24.85	0.097	[36]
Prismatic	NMC532	153	12.39	0.081	[38]
Prismatic	NMC622	50	4.90	0.098	[38]
Prismatic	NMC811	118	12.09	0.102	[38]
Prismatic	NMC9 0.5 0.5	165	20.27	0.122	[38]
18650	LFP	1.1	0.03	0.027	[37]
Prismatic	LFP	304	7.72	0.025	[38]
Prismatic	NMC811	157	14.60–15.54	0.093–0.099	[35]

As shown in Table 3, despite variations in the shape and specific elemental ratios within the cathode material, LIBs with the same cathode type tend to have similar ratios of the total gas production to the battery capacity. For example, NMC LIBs with a 100% SOC usually produce approximately 0.1 mol/Ah, whereas LFP LIBs yield around 0.025 mol/Ah. Furthermore, given that the gas generation mechanism is directly related to the TR reactions, which are theoretically the same for LIBs with identical materials, the fraction amount of each type of generated gas should also remain consistent. This consistency has been confirmed through experiments on LIBs with the same cathode material and identical elemental ratios. For example, the components of the generated gas from experiments with NMC 9 0.5 0.5 LIBs are summarized in Table 4.

Table 4. The main gas component results for NMC9 0.5 0.5 LIBs from the literature.

Cathode	CO_2 [%]	CO [%]	H_2 [%]	CH_4 [%]	C_2H_4 [%]	C_2H_6 [%]	Ref.
NMC9 0.5 0.5	24.8	41.3	21	3.9	7.4	0.86	[36]
NMC9 0.5 0.5	28.5	30.6	21.7	5.8	12.4	0.53	[36]
NMC9 0.5 0.5	24.2	40.44	20.26	3.86	7.28	0.11	[38]

From these listed experiments conducted on NMC9 0.5 0.5 LIBs, a significant correlation emerges in the composition of the main gasses generated, with CO being the most abundant, comprising approximately 40 % of the total. Additionally, CO_2 and H_2 are also prevalent, each accounting for over 20% of the gasses produced. These findings suggest that it is feasible to use data from previous experiments to predict the amount of gasses generated by TR in LIBs with the same cathode type.

Internal Pressure Evolution

With an understanding of the gas generation and the calculation of the gas generation amount, the internal pressure development could be modeled. Venting is initiated when the internal pressure of the cell surpasses a critical threshold, typically around 1900 kPa for 18650 LIBs [7]. Before that, the internal pressure P_{cell} is attributed to three principal factors, the pressure from electrolyte evaporation P_{eva}, the pressure from gas generation P_{gas}, and the originally existing pressure P_{amb}, which are represented in Equation (24) [7]:

$$P_{cell} = P_{eva} + P_{gas} + P_{amb} \tag{24}$$

P_{eva} is quantified using Antoine's equation, Equation (25) [45], which reflects how the pressure from the evaporated electrolyte escalates as the cell's temperature T_{cell} rises:

$$P_{eva} = 10^{9.4338 - \frac{1413}{-44.25 + T_{cell}}} \left[\text{Pa}\right] \tag{25}$$

Simultaneously, the pressure from gas generation within the cell, P_{gas}, is determined using the ideal gas law with Equation (26) [7]:

$$P_{gas} = \frac{n_{gas} R T_{cell}}{V_h} \tag{26}$$

Here, n_{gas} represents the moles of gas produced, R is the universal gas constant, T_{cell} is the temperature, and V_h is the volume of the headspace within the battery occupied by the vapor and generated gas.

After the internal pressure reaches the critical pressure, the safety valve is triggered to open, which releases the accumulated gasses and breaks the vapor–liquid equilibrium condition inside the cell. Based on the work of Kong et al. [7], a set of ordinary differential equations was formulated to simulate the dynamic change in the internal pressure over time.

As concluded from Equation (27), the changing rate of the internal pressure dP_{cell}/dt is attributed to the changing rates of the partial pressure from the electrolyte vapor, dP_{eva}/dt, and from the generated gasses, dP_{gas}/dt:

$$\frac{dP_{cell}}{dt} = \frac{dP_{eva}}{dt} + \frac{dP_{gas}}{dt} \tag{27}$$

Recognizing that the mass of the vapor changes due to the expulsion of the gas mixture and that the vapor temperature varies along with the cell's temperature, the rate of change in the partial pressure attributable to the electrolyte vapor is determined. This is accomplished through a differential representation of the ideal gas law, as expressed in Equation (28), with the mole mass of the electrolyte vapor represented by M_{eva}:

$$\frac{dP_{eva}}{dt} = \frac{RT_{cell}}{M_{eva} V_h} \frac{dm_{eva}}{dt} + \frac{m_{eva} R}{M_{eva} V_h} \frac{dT_{cell}}{dt} \tag{28}$$

Under the assumption that the composition of the venting mixture remains proportional, the mass flow rate of the vapor dm_{eva}/dt can be estimated using the system's overall mass loss rate, dm_{loss}/dt, and the mass fraction of the electrolyte vapor in the venting mixture, φ_{eva}, as represented in Equation (29):

$$\frac{dm_{eva}}{dt} = -\varphi_{eva} \frac{dm_{loss}}{dt} \tag{29}$$

Similarly, the rate of change in the partial pressure attributable to the generated gasses is also determined by applying a differential form of the ideal gas law with Equation (30):

$$\frac{dP_{gas}}{dt} = \frac{RT_{cell}}{V_h} \frac{dn_{gas}}{dt} + \frac{n_{gas} R}{V_h} \frac{dT_{cell}}{dt} \tag{30}$$

Unlike the mass flow rate of the electrolyte vapor, the rate of change in the amount of gasses generated from TR reactions is influenced not only by venting, but also by the continuous production of gasses from ongoing TR reactions. This dual-source contribution to the gas generation rate is captured in Equation (31):

$$\frac{dn_{gas}}{dt} = \frac{dn_{gas}}{dt}\Big|_{generation} - \frac{\varphi_{gas}}{M_{gas}} \frac{dm_{loss}}{dt} \tag{31}$$

Here, the gas generation amount $dn_{gas}/dt\big|_{generation}$ is calculated following the methodology outlined in the previous section on gas generation, and the mole mass of the generated

gasses, M_{gas}, is calculated with Equation (32) as follows. Meanwhile, the mass fraction of the gasses within the venting mixture is denoted as φ_{gas}.

$$M_{gas} = \frac{\sum_{b=1}^{6} M_{gas,b} \cdot n_{gas,b}}{n_{gas,generation}} \quad (32)$$

2.1.3. Venting Sub-Model

With the internal pressure and gas generation already acquired, the venting sub-model is then developed, which focuses on the venting dynamics, including the characterization of mass and energy losses during the venting process, with the workflow shown in Figure 5.

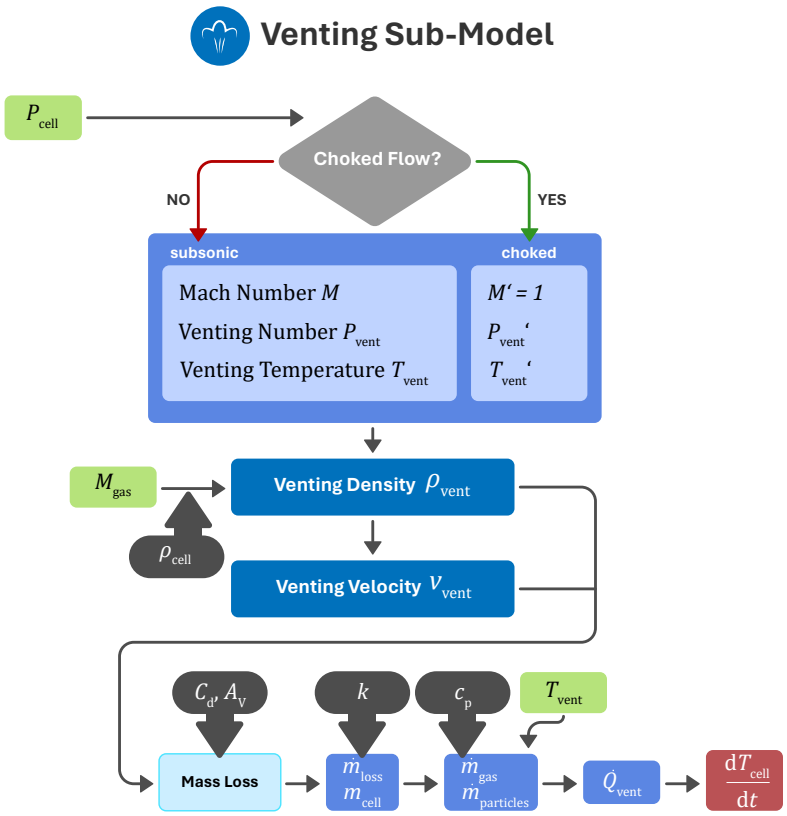


Figure 5. A flow chart of the venting sub-model.

Venting Dynamics Calculation

Based on the work of Kong et al. [7], to calculate the venting dynamics within this sub-model, the flow condition—whether subsonic or choked—first needed to be determined. The flow is considered subsonic if the ambient pressure P_{amb} is greater than a function of the internal pressure P_{cell} factored by the heat capacity ratio γ, represented in Equation (33). Otherwise, the flow is regarded as choked.

$$P_{amb} > P_{cell}\left(\frac{2}{\gamma+1}\right)^{\frac{\gamma}{\gamma-1}} \quad (33)$$

Upon establishing the flow regime, the Mach number M, venting pressure P_{vent}, venting temperature T_{vent}, and venting velocity v_{vent} can be calculated using isotropic nozzle

flow equations and the pseudo diameter approach [7,19,22,46]. If the flow is determined to be subsonic, the following equations are used:

$$M = \sqrt{\frac{2}{\gamma - 1}\left[\left(\frac{P_{\text{cell}}}{P_{\text{amb}}}\right)^{\frac{\gamma-1}{\gamma}} - 1\right]} \tag{34}$$

$$P_{\text{vent}} = P_{\text{amb}} \tag{35}$$

$$T_{\text{vent}} = T_{\text{cell}}\left(\frac{P_{\text{amb}}}{P_{\text{cell}}}\right)^{\frac{\gamma-1}{\gamma}} \tag{36}$$

If the flow is determined to be choked, the Mach number is set to 1 and the pressure and venting temperature are determined by

$$M = 1 \tag{37}$$

$$P_{\text{vent}} = P_{\text{cell}}\left(\frac{2}{\gamma + 1}\right)^{\frac{\gamma}{\gamma-1}} \tag{38}$$

$$T_{\text{vent}} = T_{\text{cell}}\left(\frac{2}{\gamma + 1}\right) \tag{39}$$

These parameters are fundamental to determining the density of the gaseous venting mixture $\rho_{\text{vent,gas}}$ with Equation (40), where $M_{\text{gas,mix}}$ is the molar mass of the gas mixture.

$$\rho_{\text{vent,gas}} = \frac{P_{\text{vent}} M_{\text{gas,mix}}}{R T_{\text{vent}}} \tag{40}$$

Mass Loss Calculation

The material ejected from a battery includes a gaseous venting mixture and solid particles. After the determination of the density of this combined ejection material, ρ_{vent}, the venting speed v_{vent} is calculated with Equation (41):

$$v_{\text{vent}} = M\sqrt{\frac{\gamma P_{\text{vent}}}{\rho_{\text{vent}}}} \tag{41}$$

The studies by Wang et al. [22] and Finegan et al. [47] break down the ejection process of the particles into four distinct stages. **(Stage I):** Initially, the battery is at rest, with the jelly roll and safety valve intact. **(Stage II)**: As TR progresses, substantial gas release raises the cell temperature, leading to a pressure differential that fractures the electrode materials. Concurrently, binder decomposition at elevated temperatures causes electrode particle debonding. These factors contribute to inter-particle fractures and the formation of gas pockets that drive the fragmented electrode materials toward the headspace. **(Stage III)**: As these materials are propelled by the gas flow, they move through newly formed channels until they are expelled into the ambient environment, particularly accelerating near the safety valve. **(Stage IV)**: This expulsion process creates channels within the gas pockets, leading to the observable collapse of the spiral-wound layers.

These mechanisms indicate that the mass flow rate of LIBs during venting is hard to describe using an exact principle, particularly concerning the ejection of solid particles. Nevertheless, experimental evidence suggests a similarity in the total mass loss rate for identical types of LIBs under well-controlled conditions [36]. The fraction of the mass loss attributed to solid particle ejection has been the focus of several studies: Coman et al. [19] performed numerous experiments under consistent conditions and utilized the

average total mass loss rate for their predictive modeling. Shen et al. [38] concentrated on quantifying the ratio of the mass of the ejected solid particles to that of the generated gasses. Recognizing the difficulty in the precise measurement and formulation of the mass flow rate of the ejected solid particles, Wang et al. [22] postulated that these rates are proportional to the total mass loss, forming the basis for their model. Accordingly, in the context of this work, we adopted the assumption that the mass flow rate of the solid particles is proportional to the total mass flow rate during venting. Under this assumption, the relationship between the mass flow rate of the ejected solid particles and that of the gas mixture can be described with the ratio k:

$$\frac{dm_{\text{particles}}}{dt} = k\frac{dm_{\text{vent,gas}}}{dt} \tag{42}$$

With $dm_{\text{loss}}/dt = dm_{\text{vent,gas}}/dt + dm_{\text{particles}}/dt$, the partial mass flow rates are determined as

$$\frac{dm_{\text{particles}}}{dt} = \frac{k}{k+1}\frac{dm_{\text{loss}}}{dt} \tag{43}$$

$$\frac{dm_{\text{vent,gas}}}{dt} = \frac{1}{k+1}\frac{dm_{\text{loss}}}{dt} \tag{44}$$

The total density of the venting mixture ρ_{vent} is then estimated with k as in Equation (45):

$$\rho_{\text{vent}} = \frac{k+1}{\frac{k}{\rho_{\text{cell}}} + \frac{1}{\rho_{\text{vent,gas}}}} \tag{45}$$

Therefore, from the density of the venting mixture, the discharge coefficient C_{d} considering the non-ideal effect, and the vent area of the cell A_v, the total mass flow rate dm_{loss}/dt can be determined with Equation (46) [7], and the partial mass flow rate can then be calculated by combining Equations (43) and (44).

$$\frac{dm_{\text{loss}}}{dt} = C_{\text{d}} A_v \rho_{\text{vent}} v_{\text{vent}} \tag{46}$$

Energy Loss Calculation

In the assessment of energy dissipation during the venting process associated with the mass loss in LIBs, the sub-model incorporates several equations to describe the energy changes due to the ejection of various materials based on the work of Coman et al. [19].

The energy required for electrolyte evaporation is absorbed from the internal energy of the battery. This heat loss is quantified by $\dot{Q}_{\text{eva}}$, as represented in Equation (47) with the mass rate of the evaporated electrolyte being $-dm_{\text{eva}}/dt$ and its latent heat of vaporization being L_{vap}.

$$\dot{Q}_{\text{eva}} = -\frac{dm_{\text{eva}}}{dt} \cdot L_{\text{vap}} \tag{47}$$

Similarly, the rate of heat loss from gas venting, $\dot{Q}_{\text{vent,gas}}$, is calculated with Equation (48) by multiplying the mass rate of the venting gas $-dm_{\text{vent,gas}}/dt$, the specific heat capacity of the gas $c_{p,\text{gas}}$, and the temperature of the venting gas T_{vent}, which reflects the heat carried away by the gasses escaping from the battery.

$$\dot{Q}_{\text{vent,gas}} = -\frac{dm_{\text{vent,gas}}}{dt} c_{p,\text{gas}} T_{\text{vent}} \tag{48}$$

For solid particle ejection, $\dot{Q}_{\text{ej}}$ denotes the rate of heat loss, calculated with Equation (49), with the specific heat capacity estimated to be the specific heat capacity of

the cell, $c_{p,\text{cell}}$. This term signifies the heat associated with the ejected solid particles as they are expelled from the cell [22].

$$\dot{Q}_{\text{ej}} = -\frac{dm_{\text{particles}}}{dt} c_{p,\text{cell}} T_{\text{vent}} \tag{49}$$

Collectively, the total rate of temperature change within the cell, dT_{cell}/dt, is derived from the sum of the heat dissipation rates due to electrolyte evaporation, gas venting, and solid particle ejection with Equation (50), providing an overarching view of how the cell's temperature is influenced by these concurrent processes during a TR event.

$$\frac{dT_{\text{cell}}}{dt} = \frac{\dot{Q}_{\text{eva}} + \dot{Q}_{\text{vent,gas}} + \dot{Q}_{\text{ej}}}{m_{\text{cell}} c_{p,\text{cell}}} \tag{50}$$

2.2. Experiment Setup

In order to ensure that the developed model could reflect the complexity of real-world scenarios, experiments were designed and conducted to validate the model in this study. The cell under test was the LG®-INR18650-MJ1, featuring NMC811 chemistry and charged to a 100% SOC for all tests. The LIB sample employed in this study had a capacity of 3.5 Ah, a mass of around 46.5 g, a diameter of 18 mm, and a length of 65 mm. The cell's electrolyte was a solvent comprising ethylene carbonate (EC), dimethyl carbonate (DMC), and propylene carbonate (PC). The anode comprised graphite containing a minor silicon content, while the principal cathode constituent was $Li_xNi_{0.83}Mn_{0.07}Co_{0.1}O_2$, as measured in previous work [48–50]. As for the trigger of TR, multiple different constant heating powers—20 W, 30 W, 50 W, 70 W, and 90 W—were applied to the battery via a 15 × 54 mm handmade NiCr wire heater fixed to the surface of the cell, either covering the bottom of the cell or vertically covering the full body of the cell, as shown in (a) and (b) in Figure 6. To monitor temperature changes with precision, four J-type thermocouples were positioned evenly across the battery surface, so the mean value from them could be taken to represent the cell temperature, as represented in (c) in Figure 6. Considering the high temperature and fast-changing rate during the TR process, mass losses were recorded using a high-resolution electronic balance only before and after the experiment, while a SIEMENS® SIWAREX WL260 SP-S AA load cell was used during the experiment to capture the real-time mass loss resulting from the TR and venting process. The fixture system and load cell are represented in Figure 7.

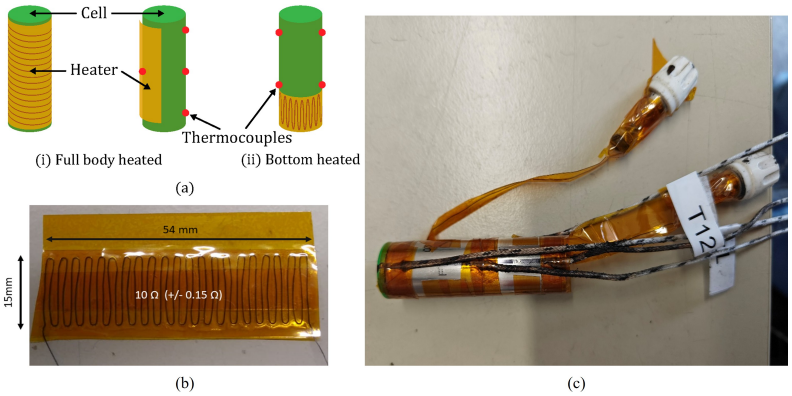


Figure 6. Heater and thermocouples used in the experiments, with (**a**) a schematic illustration of the cell, heater, and thermocouples, (**b**) an actual picture of the handmade NiCr wire heater used, and (**c**) an actual picture of the cell with the thermocouples and heater attached.

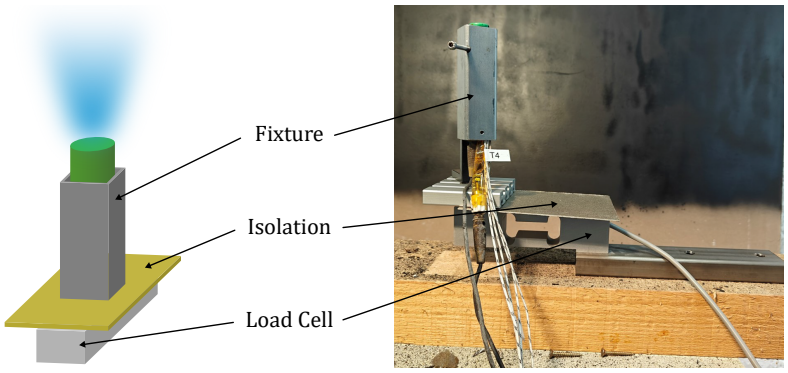


Figure 7. (**a**) Schematic illustration and (**b**) actual picture of the fixture system and the load cell used in the experiments.

A visualization system was also employed in our experiment, consisting of a high-speed camera, Cyclone-65-70, manufactured by Optronis® (Optronis GmbH, Kehl, Germany), which was capable of capturing 50 to 169 frames per second. This setup was enhanced by a light source arrangement, a laser emitting at 640 nm with a power of 10 mW or a spotlight, depending on the effect, which was used to illuminate the battery and ensure the clear visualization of the TR event as it unfolded, as shown in Figure 8.

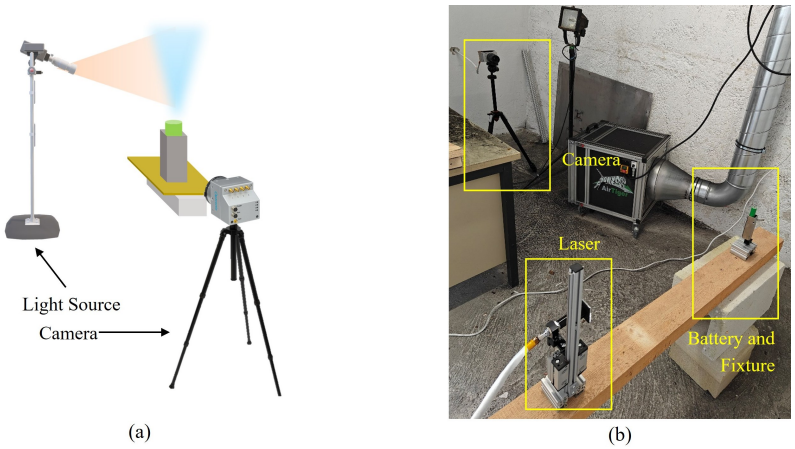


Figure 8. (**a**) Schematic illustration and (**b**) actual picture of the visualization system built for the experiments.

2.3. Simulation Setup

The LIB sample employed in this study was the NMC811 INR18650MJ1 cell from LG®, the same as was chosen for the experiment, featuring a capacity of 3.5 Ah, a mass of around 46.5 g, a diameter of 18 mm, and a length of 65 mm, with a solvent comprising EC, DMC, and PC as the electrolyte, graphite containing a minor silicon content as the anode, and $Li_xNi_{0.83}Mn_{0.07}Co_{0.1}O_2$ as the cathode. The main components of the sample used in this study align with those of the sample used in the experiments of Kriston et al. [40], allowing for the adaptation of TR reaction kinetics from their work.

The heat generated from the TR event originating from the anode, cathode, and electrolyte was calculated separately using the model. This calculation required knowledge of the mass of the anode, cathode, and electrolyte, which could not be obtained from the manufacturer. Based on Golubkov's in-lab measurements after disassembling and drying the cells [20], the mass of the anode was estimated to be 15% of the cell mass, while the cathode accounted for 26%. The mass percentage of the electrolyte, as discussed by

Lebedeva et al. [51], can affect the performance of the cell and may vary. In this study, the mass of the electrolyte involved in the reactions was estimated to be 10% of the cell mass, with the mass ratio of the composition EC:DMC:PC being 6:3:1 [48].

As for the trigger of TR, the heating power and the cut-off temperature of the external heater were set to be the same as the values in the experiment. A constant temperature boundary was applied to the outermost side of the cell, representing 12 °C air that transferred heat through convection to the cells as the only method of heat transfer with the surrounding environment considered. The temperature of the cell was considered to be homogeneously distributed in this work, while the gasses all fitted the ideal gas law and were also homogeneously distributed in the reaction volume and venting mixture.

The primary focus of parametrization work for the TR sub-model lay in determining the so-called thermal triplets: the frequency factor A, activation energy E, and heat of reaction h. These parameters have been investigated in numerous studies, employing commonly used methods such as accelerated rate calorimetry (ARC), differential scanning calorimetry (DSC), differential thermal analysis (DTA), or thermal gravimetric analysis (TGA) coupled with gas analysis [8,12,25,40,52]. In this work, Richard and Dahn's data were employed for the A1 and A2 reactions, while Kriston's data were applied for the A3, A4, and cathode reactions. The parameters are summarized in Table 5.

Table 5. The determined thermal triplets of thermal runaway.

Reaction	Description	Ref.	E(J/mol)	A(1/s)	h(J/g)
A1	SEI decomposition	[8]	1.35×10^5	1.67×10^{15}	613
A2	SEI regeneration	[8]	1.06×10^5	3.33×10^{10}	818
A3	Li–electrolyte reaction	[40]	1.62×10^5	1.78×10^{14}	479
A4	Binder decomposition	[40]	9.35×10^4	5.62×10^6	208
C1	NMC decomposition	[40]	1.41×10^5	3.22×10^{10}	100
C2	Electrolyte evaporation	[40]	9.51×10^4	2.23×10^7	−625
	Electrolyte combustion		1.26×10^5	5.14×10^{18}	20,000
	Electrolyte decomposition		2.28×10^6	5.14×10^{25}	155
C3	NMC binder decomposition	[40]	2.05×10^5	3.78×10^{12}	213
C4	Further decomposition of NMC, oxygen reactions	[40]	2.89×10^5	1.30×10^{16}	189

As for the prediction of gas generation, the generation amount parameters ω_{ab} used in matrix $\omega_{a,b}$ in Equation (22) were estimated based on the experiment result with the same LIB cathode material NMC811 from the work by Shen et al. [38]. Using the approaches for TR reactions and the parameters considered in this work, the matrix $\omega_{a,b}$ was then modified to the matrix in Equation (51):

$$\begin{pmatrix} \Delta x_{\mathrm{A1}} \\ \Delta x_{\mathrm{A3}} \\ \Delta x_{\mathrm{A4}} \\ \Delta x_{\mathrm{C2}} \\ \Delta x_{\mathrm{C3}} \end{pmatrix}^{T} \begin{pmatrix} 0.275 & 0 & 0 & 0 & 0 & 0 \\ 0.033 & 0.080 & 0 & 0.190 & 0.055 & 0.002 \\ 0 & 0 & 0.025 & 0 & 0 & 0 \\ 0.033 & 0 & 0 & 0 & 0 & 0 \\ 0 & 0 & 0.060 & 0 & 0 & 0 \end{pmatrix} = (\Delta n_{\mathrm{CO_2}}, \Delta n_{\mathrm{CO}}, \Delta n_{\mathrm{H_2}}, \Delta n_{\mathrm{CH_4}}, \Delta n_{\mathrm{C_2H_4}}, \Delta n_{\mathrm{C_2H_6}}) \quad (51)$$

The mass flow rate fraction ratio was obtained by fitting the simulation result with the experiment results, while the estimation of other parameters for the internal pressure sub-model and venting sub-model took reference from [7,53], where 18650 types of LIB were also studied. The principle parameters and the values are listed in the following Table 6.

Table 6. The venting and thermodynamic parameters adopted in the model.

Parameters	Value	Unit	Ref.
c_p	0.83	$Jg^{-1}K^{-1}$	[53]
A_v	9.8	mm^2	[7]
V_h	1.158	cm^3	[7]
C_d	0.8	-	[7]
γ	1.4	-	[7]
φ_{eva}	0.06	-	Fit
φ_{gas}	0.12	-	Fit
k	4.8	-	Fit

3. Results and Discussion

In this section, the results of the experiments and simulations with LG MJ1 batteries are presented and discussed. The outcomes from the simulations are compared with the experimental results from our study and the existing literature, and this comparison evaluates the employed modeling approaches in terms of their precision and robustness in predicting the multifaceted behaviors of TR in LIBs.

3.1. Experiment Results

3.1.1. Thermal Runaway Evolution

The entire TR process was recorded using the visualization system in the experiments. The phases of thermal runaway observed in an experiment with a 20 W vertically attached heater are presented in Figure 9, while the corresponding temperature–mass change curve is shown in Figure 10.

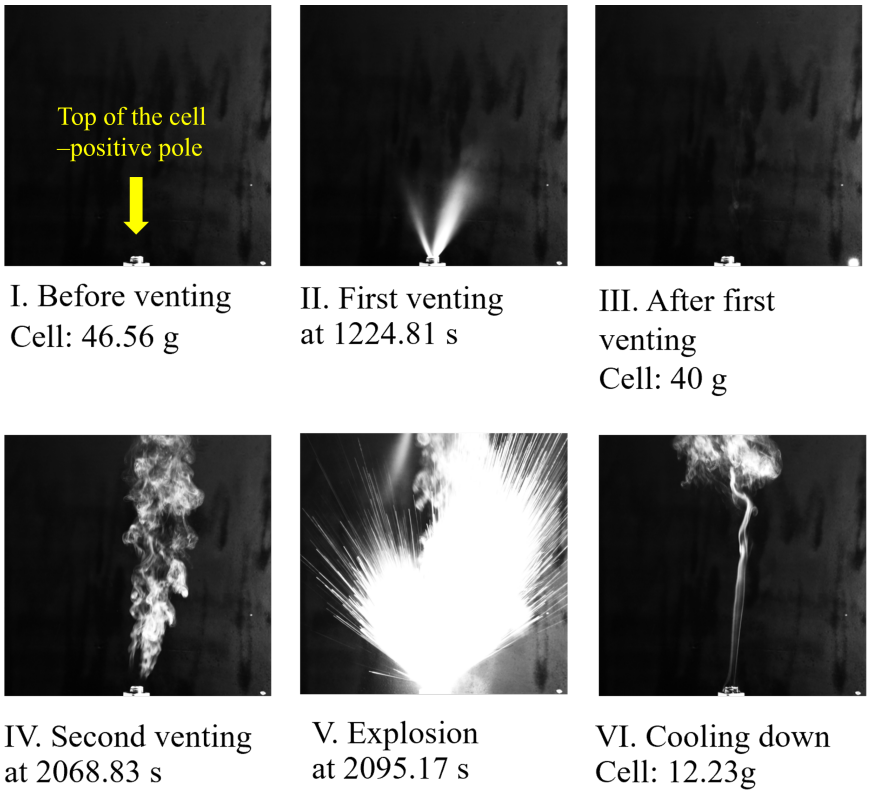


Figure 9. The recorded thermal runaway process from one experiment with a 20 W vertically attached heater.

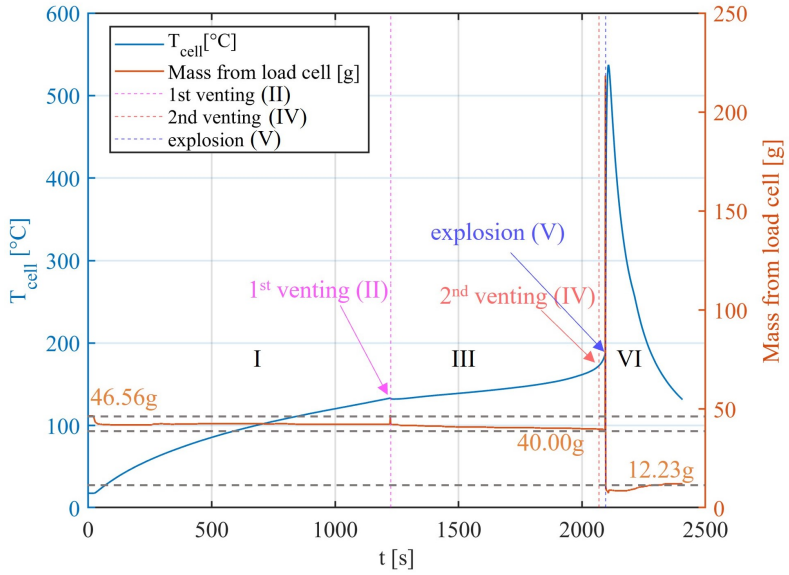


Figure 10. The recorded cell temperature and mass changes from one experiment with a 20 W vertically attached heater.

Here, two distinct venting events were observed. The first venting event (Stage II in Figure 9) was noticeable at the early heating stage, occurring at approximately 120 °C. It was marked by the opening of the safety valve, which coincided with a minor mass loss, 14% of the total battery mass, and a dip in the temperature, reflecting the release of pressure and thermal energy from the cell. Following this venting episode, the battery entered a relatively stable phase (Stage III), where no further obvious venting behaviors were observed. However, the energy released by the venting was not able to stop the progression of TR, as the cell temperature continued to rise, while the generation of gasses continued within the battery. Subsequently, the second venting event (Stage IV) happened just before the TR caused the cell to burst, at a stage where the battery already exhibited an elevated internal pressure and temperature. This venting was considerably more intense, rapidly followed by an explosion (Stage V), where the TR process reached a peak. The explosion ejected a large amount of particles, and the resulting impact caused the load cell to oscillate up and down, thereby recording highly fluctuating pressure values, making it impossible to read the data at that moment. Once the load cell stabilized, the recorded readings indicated a significant mass loss of 60%. Following this phase, the TR process concluded swiftly, and the battery transitioned into the cooling down stage (Stage VI), characterized by a rapid decrease in the temperature.

The temperature at which a cell undergoes TR, known as the onset temperature, is a crucial parameter to identify, as it marks the point at which the cell's temperature begins to rise uncontrollably. Understanding this temperature enables the development of safety strategies designed to prevent further damage and mitigate the risks associated with TR. Similarly, the peak temperature reached during a TR event is a vital parameter to record, as it indicates the maximum severity of the thermal event and its potential consequences. Knowing the peak temperature allows for the evaluation of safety margins, the testing of the material's thermal stability, and the optimization of thermal management systems to withstand extreme conditions. Therefore, both the onset and peak temperatures in each experiment in this study were recorded and summarized, as shown in Figure 11.

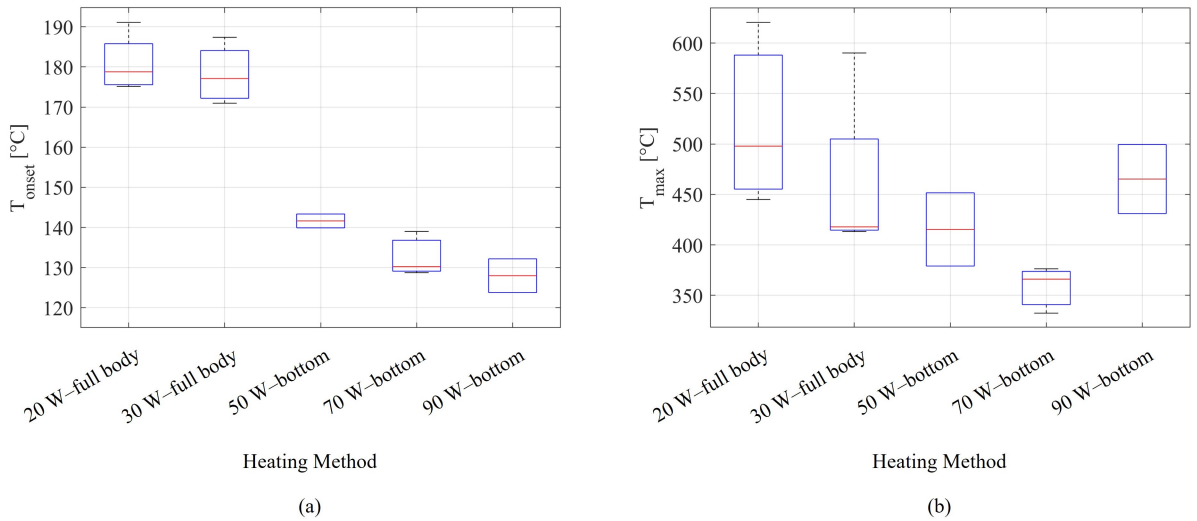


Figure 11. Box plot of the recorded (**a**) onset temperature and (**b**) peak temperatures from the experiments with LG MJ1 batteries in this study. Here, the box portion covers data from the 25th percentile to the 75th percentile, with a central line marking the median value. Lines extend from each box to the minimum and maximum values to capture the range of the remaining data.

Part (a) of Figure 11 presents a box plot of the onset temperatures T_{onset} recorded from the experiments. The experiments using the full-body heating method exhibited similar median onset temperatures around 180 °C, with the onset temperatures generally being lower for experiments conducted at a higher heating power (30 W). In contrast, the results from the bottom-heating methods showed significantly lower onset temperatures compared to the full-body heating methods, with the onset temperatures decreasing further as the heating power increased. These observations indicate that both localized heating at the bottom and the application of higher heating power accelerate the onset of TR, triggering TR at lower temperatures.

The peak temperature results, T_{max}, are presented as a box plot in part (b) of Figure 11. The experiments using the full-body heating methods at 20 W and 30 W demonstrated higher peak temperatures, with median values around 500 °C and 450 °C, and showed a wider range of temperature variation. In comparison, the bottom-heating methods (50 W, 70 W, and 90 W) produced lower peak temperatures, with median values between 350 °C and 400 °C. This suggests that localized heating at the bottom produces less severe TR outcomes, characterized by lower maximum temperatures reached during TR events.

The results show that both the onset and peak temperatures are significantly affected by the heating method and power level, which aligns well with the work by Willstrand et al. [35], where the onset temperature was at around 150 °C, while the peak temperature varied from 450 °C to 900 °C. Full-body heating results in higher onset and peak temperatures, indicating a more intense and uniform thermal reaction throughout the battery. In contrast, bottom heating triggers TR at lower onset temperatures and results in lower peak temperatures, suggesting that TR events occur earlier but are less severe. This difference can be attributed to the uniform heat distribution provided by the full-body heating method, which takes longer to reach the critical temperature but causes the entire battery to undergo a more severe TR event simultaneously. Additionally, since the simulation used a lumped model that approximated the heating method as an equivalent to full-body heating, this section will also include a comparison and discussion of the simulation results with the experimental findings.

Besides the temperature, the mass loss from a TR event is also a key parameter to quantify, as it indicates both the severity of the venting event and the extent of material

degradation within the battery. This information helps in identifying the specific components most susceptible to degradation, allowing for the optimization of battery designs to reduce the likelihood of venting or to control the release of materials more safely. Additionally, mass loss data provide valuable input for refining predictive models of TR behavior by offering more detailed and accurate information. Consequently, the mass loss fractions observed in the experiments were carefully measured and are summarized as a box plot in Figure 12.

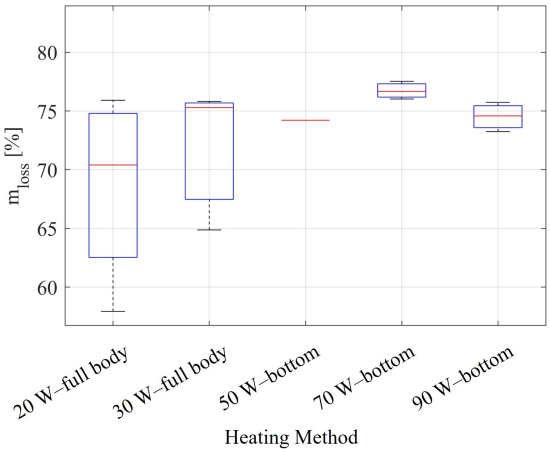


Figure 12. Box plot of the recorded mass loss fractions from the experiments with LG MJ1 batteries in this study. Here, the box portion covers data from the 25th percentile to the 75th percentile, with a central line marking the median value. Lines extend from each box to the minimum and maximum values to capture the range of the remaining data. There is no box for the result of the experiment with 50 W bottom heating, because there was just once experiment recorded.

The median mass loss fractions from all experiments, regardless of the heating method, were within the range of 70% to 77% regarding the initial cell mass. The full-body heating method showed greater variability in the mass loss, from approximately 60% to 75% with 20 W heating power and from 65% to 75% with 30 W. This variability was likely due to the uniform heating of the entire cell, leading to varying venting dynamics. In contrast, the bottom-heating method showed a more consistent mass loss fraction, with values ranging from 76% to 77% at 70 W and from 74% to 76% at 90 W, indicating that localized heating results in a more predictable pattern of material degradation and venting. This outcome is highly consistent with the findings reported by Fedoryshyna et al. and Gillich et al. [33,34], where the mass loss rate from TR tests with 18650 MJ1 cells ranged from 55% to 85%, with a median value of 75%. These relatively narrow mass loss fractions not only validate the reliability of our experimental results but also facilitate a more straightforward assumption of a specific mass loss rate in modeling work, which in turn reduces the complexity and unpredictability associated with venting behavior during TR events.

The standard deviation of the experiment results can be seen in the following table, Table 7.

Here, the standard deviations of the results from each heating method were similar. Although the standard deviation was smaller in experiments with higher heating power, we frequently observed that either heating power exceeding 30 W or the bottom-heating method could cause localized high temperatures. This would lead to a localized TR event, resulting in a significant amount of material being ejected through the newly formed breach. Consequently, the typical venting process we aimed to study could not be observed. Therefore, despite the relatively high standard deviation in the results, we selected the case with the 20 W full-body heating method for further simulation and study.

Table 7. The standard deviation of the experiment results.

Heating Method	STD of T_{onset} (°C)	STD of T_{max} (°C)	STD of m_{loss}
20 W	5.81	66.63	7%
30 W	6.45	75.37 [1] (1.41 [2])	5%
50 W	1.72	36.31	0%
70 W	4.53	18.77	1%
90 W	4.20	34.24	1%

[1] With the consideration of the outlier. [2] Without the consideration of the outlier.

3.1.2. Venting Analysis with Load Cell

The load cell used in our experiments acted as a pressure sensor, capturing data that reflected both the actual mass of the battery and the recoil force F_{recoil} generated during venting events. A schematic illustration of this force relationship is provided in part (a) of Figure 13. An accurate mass reading from a load cell is only possible when the system is in equilibrium. However, during venting events, particularly in the intense second venting phase, a substantial recoil force is generated due to the rapid ejection of materials, causing the recorded value to significantly exceed the gravitational force of the battery. To interpret the load cell data, we assume that the mass flow rate $\dot{m}$ remains constant during these brief venting intervals, enabling us to estimate both the battery's mass and the corresponding recoil force. This estimation is crucial for determining the venting speed, which is calculated using the principle of the conservation of momentum, as described by Equation (52). The results of the estimation for the actual battery mass and venting speed are also represented in part (b) of Figure 13.

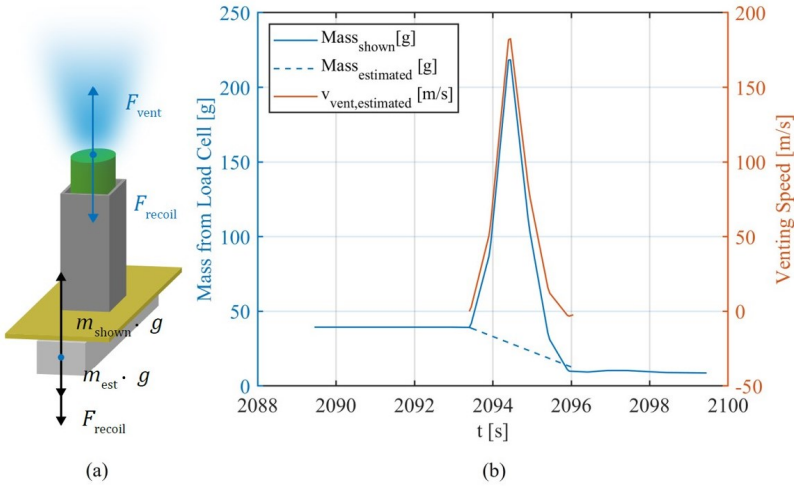


Figure 13. Force analysis for a venting event and the result from the load cell, with (**a**) a schematic illustration of force analysis and (**b**) the shown and estimated mass and estimated venting speed data from the load cell.

$$F_{vent} = F_{recoil} = \dot{m} v_{vent} \tag{52}$$

From the data collected, the maximum venting speed was estimated to be 180 m/s. The load cell recorded a mass loss of 34.33 g (74 %), which closely matched the balance measurement of 34.31 g (74%). This strong agreement between the load cell and balance measurements largely supports the assumptions made regarding the mass flow rate and recoil force during the venting process. However, the inherent randomness of TR and venting events causes significant oscillations in the recoil force, leading to occasional discrepancies between the load cell readings and the balance measurements, which is also shown in the results from the literature [33–35]. This suggests that while a load cell can

be a useful tool, further refinement of the experimental setup is necessary to improve its reliability, which could be an important focus for future work.

3.2. Simulation Results

3.2.1. Thermal Runaway Parameters

The simulation results offer a detailed perspective on the TR behavior of an LG MJ1 battery, highlighting the evolution of the temperature, mass loss, and venting speed. Figure 14 illustrates the simulated progression of these parameters during TR in an LG MJ1 battery. The simulation was configured with a trigger method using a 20 W heater operating at 55% efficiency, continuously heating the battery until it reached 200 °C, in order to replicate the experimental setup conditions. However, it is important to note that the experimental setup involved significant heat loss, which was not fully accounted for in the simulation. After calibrating the simulation with the experimental data, it was assumed that the mass flow rate of the solid particles was 4.8 times that of the gas mixture.

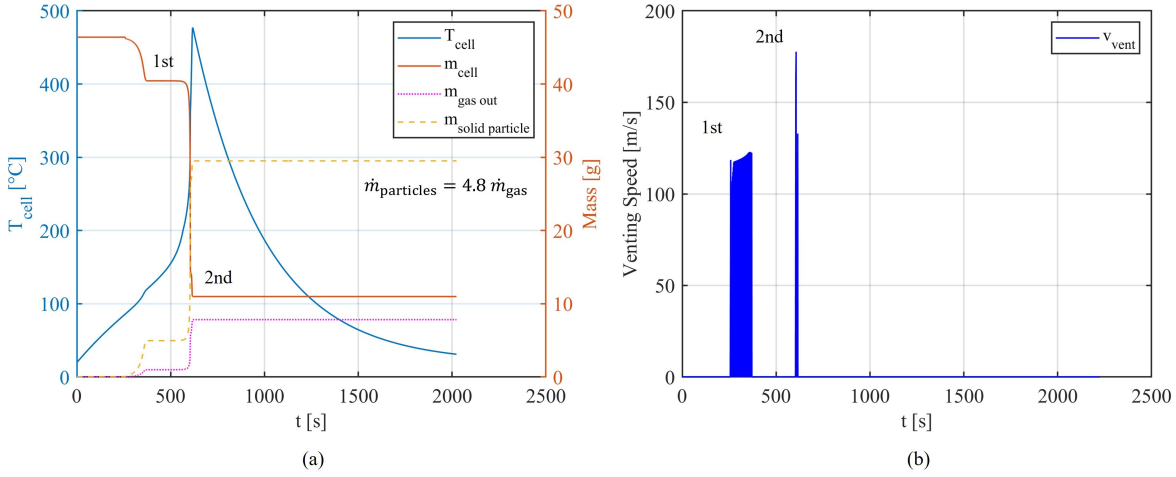


Figure 14. Evolution of temperature and mass (**a**), as well as venting speed (**b**), during thermal runaway in LG MJ1 battery in simulation with 20 W heater.

As shown in Figure 14, the simulation identified two distinct venting phases, closely mirroring the experimental observations. Part (a) shows that the first venting event was characterized by a smaller mass loss of 13%, occurring at a lower temperature from 90 °C to 120 °C, which aligns with the early stage of TR shown in the experiment. The second, more significant venting phase is shown to have started under conditions of a higher temperature and pressure, followed by a burst caused by TR with a substantial mass loss of 61%. From the venting speed result in part (b), we can see that this second venting also reached a maximum venting speed of approximately 180 m/s, aligning well with the estimated experimental data.

A detailed comparison between the simulation results and experimental data is presented in Figure 15, revealing a strong correlation, particularly in the temperature changes during the TR process. The peak temperatures recorded in the simulation and experiment were 478.3 °C and 473.0 °C, respectively, showing a difference of only 1%, and were within the range of our other experiment results. Similarly, the onset temperatures are 183.8 °C in the simulation and 176.6 °C in the experiment, with a difference of 4%, which also aligns greatly with our other experiment results. However, the experimental results exhibited time delays of approximately 250 s in key features, such as the first venting event, TR onset, and peak temperatures, compared to the simulation. These delays can be attributed to the simplifications inherent in the lumped model used in the simulation, such as the omission of internal heat transfer within the cell, as well as heat loss in the experimental setup that

was not fully accounted for in the simulation. Despite these discrepancies, the overall temporal progression from the first venting event to the onset of TR showed significant similarity, with 179 s in the experiment and 188 s in the simulation. This consistency demonstrates the predictive capability of the model, confirming its utility in simulating TR behavior.

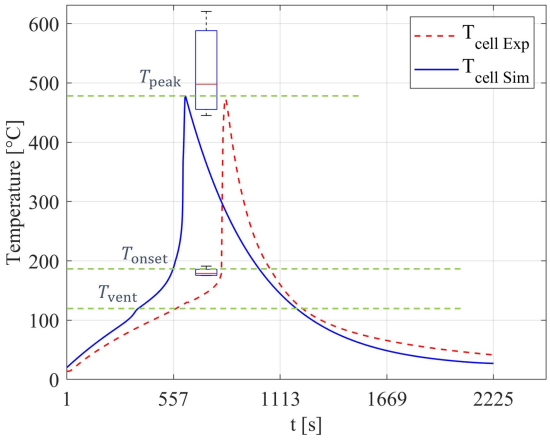


Figure 15. Temperature evolution curve during thermal runaway in an LG MJ1 battery in the simulation (blue line) and one experiment with a 20 W heater (red dots), with the box plots of the peak and onset temperature from all the experiments conducted in this study with the 20 W full-body heating method.

The mass loss figures obtained using both the simulation and experimental methods further demonstrated a strong correlation, with both showing a mass loss of approximately 74%. This value aligns closely with the mass loss percentages recorded in our other experiments conducted with fully charged LG MJ1 batteries. Such consistency across different tests strengthens the validity of the proportional assumption used in the simulation, specifically the assumption regarding the mass loss from solid particle ejection relative to the total mass loss.

These similarities between the experimental and simulated results validate the effectiveness of the simulation model. The model's ability to replicate these critical aspects of the TR process indicates that it accurately reflects the dynamics occurring within the battery during TR events.

3.2.2. Gas Generation Analysis

As shown in part (a) of Figure 16, the gas generation result from the simulation indicated that H_2, CO_2, and CO were the primary gasses produced, with different patterns in their timing and quantity of release represented in part (b), which fits with the gas generation matrix (22) implemented.

During the first venting phase, CO_2 was predominantly generated. This early release aligned with SEI decomposition, which started at around 90 °C and produced CO_2. It is also shown from the simulation result that while CO_2 emerged first, the majority of other gasses, including H_2 and CO, were released during the second venting event. This phase corresponded with ongoing TR reactions, especially the Li–electrolyte reaction, from which most gasses were sourced.

A comparative analysis of the gas generation results from this simulation and the experimental studies reported in the literature [38] is represented in Figure 17.

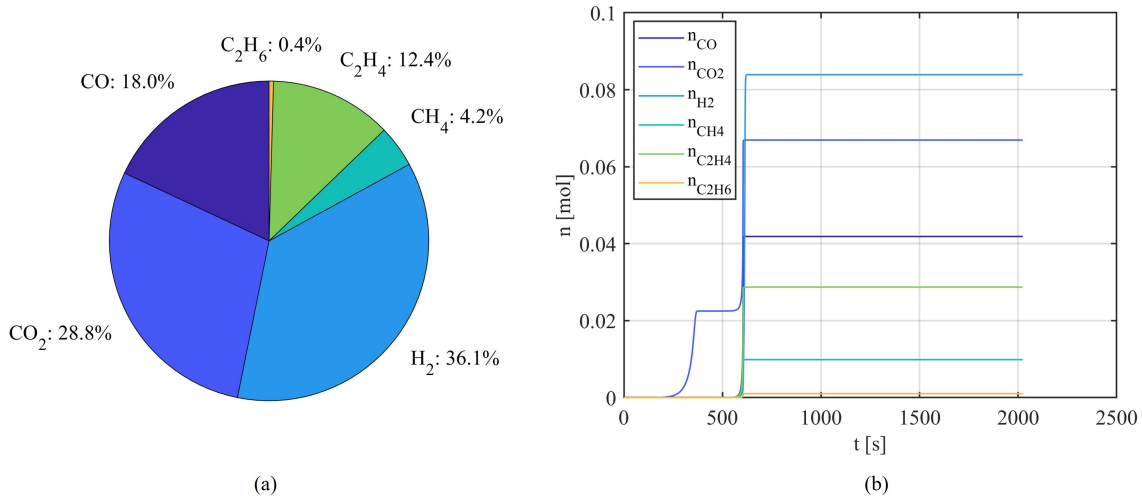


Figure 16. Gas generation during thermal runaway in an LG MJ1 battery in our simulation with a 20 W heater, with the results for (**a**) the composition of the generated gasses and (**b**) the evolution of the accumulated amount of the generated gasses.

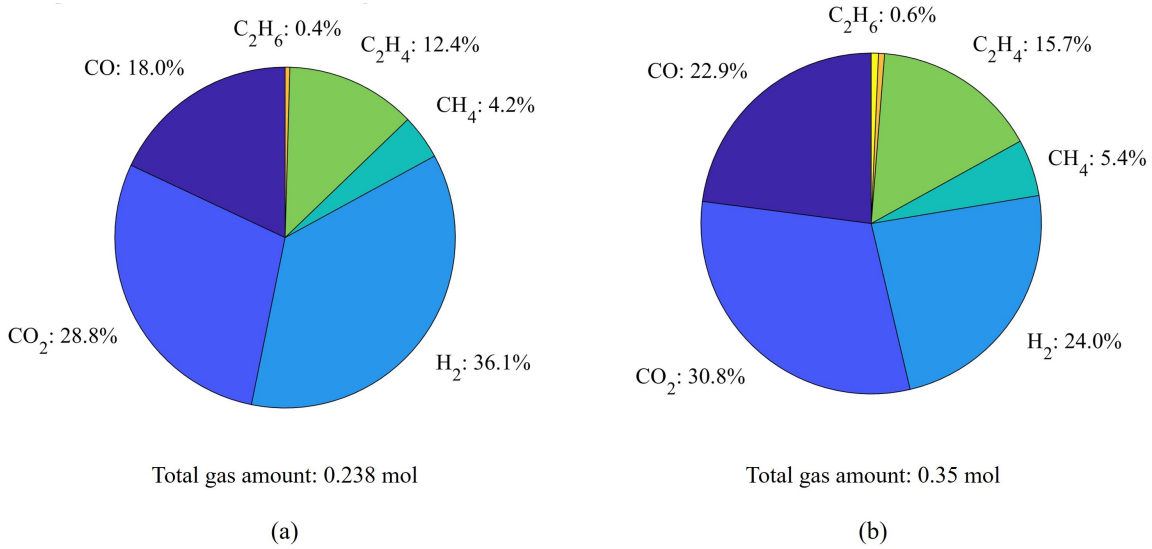


Figure 17. Composition of the gasses generated during thermal runaway in an NMC 811 battery in (**a**) a simulation in this work with a total amount of 0.238 mol and (**b**) Ref. [38] with a total amount of 0.35 mol.

The experimental findings of Shen et al. [38] indicate higher levels of CO_2 and CO production, along with a greater overall gas volume, compared to the simulation outcomes from our study. Specifically, our simulations generated a total of 0.238 mol of gasses, while the literature, assuming that the gas generation is proportional to the battery capacity (as discussed in Section 2.1.2), predicts a theoretical output of 0.350 mol. Although there is a noticeable discrepancy, the strong correlation between our simulation results and the experimental data supports the validity of the assumptions regarding the quantity of gas generated. Nevertheless, the noted differences also highlight potential limitations in the current modeling approach that may require further refinement to enhance the accuracy of the model.

1. Simplified Reaction Modeling: Only the primary gas generation reactions are considered in the modeling approach, with the omission of the complex secondary reactions that occur at higher temperatures and that can produce additional gasses, particularly

CO_2 and CO. This simplification likely contributed to the lower total gas output in the simulation.

2. Heating Power and TR Completion: The simulation possibly employed a lower heating power, insufficient to fully drive the battery through all the reactions in TR. This would naturally result in less gas generation as the TR reactions contributing to gas production would not fully develop or reach their peak activity.

These findings highlight the need to adjust the simulation parameters by incorporating a broader range of chemical interactions and thermal effects. Such improvements could ensure that future simulations align more closely with empirical data, thereby providing more reliable predictions for safety assessments and battery design optimizations.

4. Conclusions

In this work, a comprehensive model was developed and validated to simulate TR and venting processes in 18650 NMC LIBs. The model successfully captures key elements of TR, such as the temperature evolution, internal pressure changes, venting phases, and mass loss dynamics. Its validity was confirmed through experiments with LG®-INR18650-MJ1 cells, demonstrating a strong correlation with the experimental results. Notably, the model replicates critical aspects such as the double venting mechanisms, gas generation, and mass loss characteristics observed during TR events. Accurately modeling these mechanisms is crucial for understanding and mitigating TR risks. A key novelty of this study is the confirmation of proportional relationships, specifically modeling the gas generation as proportional to the cell capacity and the mass loss from solid particle ejection as proportional to the total mass loss. These simplified approaches enhance the practicality of modeling TR behaviors without compromising accuracy, suggesting a promising direction for future research efforts.

While the current model offers significant insights into the TR process, there are areas where the model could be further refined. Potential areas for further research include incorporating a more detailed treatment of internal heat transfer and expanding the range of chemical reactions considered, experimental studies to determine the kinetics of TR reactions and provide evaluations for adjusting the parameters and equations used in the model, the quantitative analysis of gas generation during TR, the accurate measurement of the venting velocity and the recording of the mass loss evolution, and the development of higher dimensional models that encompass more detailed information. These enhancements would provide a more accurate representation of the TR process, particularly in predicting gas generation, and thereby improve the simulation of the venting process.

In conclusion, this work contributes to a deeper understanding of TR in LIBs by clarifying the gas generation and venting mechanisms involved. The findings presented here provide a solid foundation for future research focused on improving battery safety, which is essential for the widespread adoption of this key technology in sustainable energy applications, supporting the global shift towards more sustainable and environmentally friendly energy solutions.

Author Contributions: Conceptualization, A.C. and A.F.; methodology, A.C.; software, A.C.; validation, A.C., R.S., M.S. and A.F.; formal analysis, A.C.; investigation, A.C. and R.S.; resources, A.F.; data curation, A.C.; writing—original draft preparation, A.C.; writing—review and editing, R.S., M.S., T.K., S.H. and A.F.; visualization, A.C.; supervision, A.F.; project administration, A.F.; funding acquisition, A.F. All authors have read and agreed to the published version of the manuscript.

Funding: This research received no external funding.

Data Availability Statement: The data can be shared upon request.

Acknowledgments: The authors thank Johann Schimon for the graphic editing of Figures 1–8, and 13.

Conflicts of Interest: Authors Marco Ströbel and Alexander Fill were employed by the company MAP Battery Tests GmbH. Authors Thomas Kottke and Stefan Hecker were employed by the company Rolls-Royce Power Systems. The remaining authors declare that the research was conducted in the absence of any commercial or financial relationships that could be construed as a potential conflict of interest.

Abbreviations

The following abbreviations are used in this manuscript:

LIB	Lithium-ion battery
SIB	Sodium-ion battery
EV	Electric vehicle
TR	Thermal runaway
ARC	Accelerated rate calorimetry
SEI	Solid electrolyte interphase
NMC	Nickel manganese cobalt oxide
LCO	Lithium cobalt oxide
LFP	Lithium iron phosphate
NCA	Lithium nickel cobalt aluminum oxide
SOC	State of charge
PVDF	Polyvinylidene fluoride
EC	Ethylene carbonate
DMC	Dimethyl carbonate
PC	Propylene carbonate
LD	Linear dichroism
STD	Standard deviation

References

1. Wang, Q.; Mao, B.; Stoliarov, S.I.; Sun, J. A Review of Lithium Ion Battery Failure Mechanisms and Fire Prevention Strategies. *Prog. Energy Combust. Sci.* **2019**, *73*, 95–131. [CrossRef]
2. Abada, S.; Marlair, G.; Lecocq, A.; Petit, M.; Sauvant-Moynot, V.; Huet, F. Safety Focused Modeling of Lithium-Ion Batteries: A Review. *J. Power Sources* **2016**, *306*, 178–192. [CrossRef]
3. Fleischhammer, M.; Waldmann, T.; Bisle, G.; Hogg, B.I.; Wohlfahrt-Mehrens, M. Interaction of Cyclic Ageing at High-Rate and Low Temperatures and Safety in Lithium-Ion Batteries. *J. Power Sources* **2015**, *274*, 432–439. [CrossRef]
4. Tran, M.K.; Mevawalla, A.; Aziz, A.; Panchal, S.; Xie, Y.; Fowler, M. A Review of Lithium-Ion Battery Thermal Runaway Modeling and Diagnosis Approaches. *Processes* **2022**, *10*, 1192. [CrossRef]
5. Shan, T.; Wang, Z.; Zhu, X.; Wang, H.; Zhou, Y.; Wang, Y.; Zhang, J.; Sun, Z. Explosion Behavior Investigation and Safety Assessment of Large-Format Lithium-Ion Pouch Cells. *J. Energy Chem.* **2022**, *72*, 241–257. [CrossRef]
6. Wang, H.; Xu, H.; Zhang, Z.; Wang, Q.; Jin, C.; Wu, C.; Xu, C.; Hao, J.; Sun, L.; Du, Z.; et al. Fire and Explosion Characteristics of Vent Gas from Lithium-Ion Batteries after Thermal Runaway: A Comparative Study. *eTransportation* **2022**, *13*, 100190. [CrossRef]
7. Kong, D.; Wang, G.; Ping, P.; Wen, J. A Coupled Conjugate Heat Transfer and CFD Model for the Thermal Runaway Evolution and Jet Fire of 18650 Lithium-Ion Battery under Thermal Abuse. *eTransportation* **2022**, *12*, 100157. [CrossRef]
8. Richard, M.N.; Dahn, J.R. Accelerating Rate Calorimetry Study on the Thermal Stability of Lithium Intercalated Graphite in Electrolyte. I. Experimental. *J. Electrochem. Soc.* **1999**, *146*, 2068. [CrossRef]
9. Richard, M.N.; Dahn, J.R. Accelerating Rate Calorimetry Study on the Thermal Stability of Lithium Intercalated Graphite in Electrolyte. II. Modeling the results and predicting differential scanning calorimeter curves. *J. Electrochem. Soc.* **1999**, *146*, 2078. [CrossRef]
10. Chen, H.; Buston, J.E.H.; Gill, J.; Howard, D.; Williams, R.C.E.; Read, E.; Abaza, A.; Cooper, B.; Wen, J.X. A Simplified Mathematical Model for Heating-Induced Thermal Runaway of Lithium-Ion Batteries. *J. Electrochem. Soc.* **2021**, *168*, 010502. [CrossRef]
11. Coman, P.T.; Darcy, E.C.; White, R.E. Simplified Thermal Runaway Model for Assisting the Design of a Novel Safe Li-Ion Battery Pack. *J. Electrochem. Soc.* **2022**, *169*, 040516. [CrossRef]

12. Hatchard, T.D.; MacNeil, D.D.; Basu, A.; Dahn, J.R. Thermal Model of Cylindrical and Prismatic Lithium-Ion Cells. *J. Electrochem. Soc.* **2001**, *148*, A755. [CrossRef]
13. Kim, G.H.; Pesaran, A.; Spotnitz, R. A Three-Dimensional Thermal Abuse Model for Lithium-Ion Cells. *J. Power Sources* **2007**, *170*, 476–489. [CrossRef]
14. Kong, D.; Wang, G.; Ping, P.; Wen, J. Numerical Investigation of Thermal Runaway Behavior of Lithium-Ion Batteries with Different Battery Materials and Heating Conditions. *Appl. Therm. Eng.* **2021**, *189*, 116661. [CrossRef]
15. Li, W.; Wang, H.; Ouyang, M.; Xu, C.; Lu, L.; Feng, X. Theoretical and Experimental Analysis of the Lithium-Ion Battery Thermal Runaway Process Based on the Internal Combustion Engine Combustion Theory. *Energy Convers. Manag.* **2019**, *185*, 211–222. [CrossRef]
16. Lopez, C.F.; Jeevarajan, J.A.; Mukherjee, P.P. Characterization of Lithium-Ion Battery Thermal Abuse Behavior Using Experimental and Computational Analysis. *J. Electrochem. Soc.* **2015**, *162*, A2163–A2173. [CrossRef]
17. Zhang, Y.; Mei, W.; Qin, P.; Duan, Q.; Wang, Q. Numerical Modeling on Thermal Runaway Triggered by Local Overheating for Lithium Iron Phosphate Battery. *Appl. Therm. Eng.* **2021**, *192*, 116928. [CrossRef]
18. Weber, N.; Schuhmann, S.; Tübke, J.; Nirschl, H. Chemical Thermal Runaway Modeling of Lithium-Ion Batteries for Prediction of Heat and Gas Generation. *Energy Technol.* **2023**, *11*, 2300565. [CrossRef]
19. Coman, P.T.; Rayman, S.; White, R.E. A Lumped Model of Venting during Thermal Runaway in a Cylindrical Lithium Cobalt Oxide Lithium-Ion Cell. *J. Power Sources* **2016**, *307*, 56–62. [CrossRef]
20. Golubkov, A.W.; Fuchs, D.; Wagner, J.; Wiltsche, H.; Stangl, C.; Fauler, G.; Voitic, G.; Thaler, A.; Hacker, V. Thermal-Runaway Experiments on Consumer Li-ion Batteries with Metal-Oxide and Olivin-Type Cathodes. *RSC Adv.* **2014**, *4*, 3633–3642. [CrossRef]
21. Zou, K.; He, K.; Lu, S. Venting Composition and Rate of Large-Format LiNi0.8Co0.1Mn0.1O2 Pouch Power Battery during Thermal Runaway. *Int. J. Heat Mass Transf.* **2022**, *195*, 123133. [CrossRef]
22. Wang, G.; Kong, D.; Ping, P.; Wen, J.; He, X.; Zhao, H.; He, X.; Peng, R.; Zhang, Y.; Dai, X. Revealing Particle Venting of Lithium-Ion Batteries during Thermal Runaway: A Multi-Scale Model toward Multiphase Process. *eTransportation* **2023**, *16*, 100237. [CrossRef]
23. Mao, B.; Zhao, C.; Chen, H.; Wang, Q.; Sun, J. Experimental and Modeling Analysis of Jet Flow and Fire Dynamics of 18650-Type Lithium-Ion Battery. *Appl. Energy* **2021**, *281*, 116054. [CrossRef]
24. Bilyaz, S.; Marr, K.C.; Ezekoye, O.A. Modeling of Thermal Runaway Propagation in a Pouch Cell Stack. *Fire Technol.* **2020**, *56*, 2441–2466. [CrossRef]
25. Ren, D.; Liu, X.; Feng, X.; Lu, L.; Ouyang, M.; Li, J.; He, X. Model-Based Thermal Runaway Prediction of Lithium-Ion Batteries from Kinetics Analysis of Cell Components. *Appl. Energy* **2018**, *228*, 633–644. [CrossRef]
26. Kriston, A.; Podias, A.; Adanouj, I.; Pfrang, A. Analysis of the effect of thermal runaway initiation conditions on the severity of thermal runaway—numerical simulation and machine learning study. *J. Electrochem. Soc.* **2020**, *167*, 090555. [CrossRef]
27. Mei, W.; Liu, Z.; Wang, C.; Wu, C.; Liu, Y.; Liu, P.; Xia, X.; Xue, X.; Han, X.; Sun, J.; et al. Operando monitoring of thermal runaway in commercial lithium-ion cells via advanced lab-on-fiber technologies. *Nat. Commun.* **2023**, *14*, 5251. [CrossRef]
28. Pegel, H.; Schaeffler, S.; Jossen, A.; Sauer, D.U. Extensive experimental thermal runaway and thermal propagation characterization of large-format tabless cylindrical lithium-ion cells with aluminum housing and laser welded endcaps. *J. Electrochem. Soc.* **2023**, *170*, 120512. [CrossRef]
29. Kennedy, R.W.; Marr, K.C.; Ezekoye, O.A. Gas Release Rates and Properties from Lithium Cobalt Oxide Lithium Ion Battery Arrays. *J. Power Sources* **2021**, *487*, 229388. [CrossRef]
30. Kim, J.; Mallarapu, A.; Finegan, D.P.; Santhanagopalan, S. Modeling Cell Venting and Gas-Phase Reactions in 18650 Lithium Ion Batteries during Thermal Runaway. *J. Power Sources* **2021**, *489*, 229496. [CrossRef]
31. Ostanek, J.K.; Li, W.; Mukherjee, P.P.; Crompton, K.; Hacker, C. Simulating Onset and Evolution of Thermal Runaway in Li-ion Cells Using a Coupled Thermal and Venting Model. *Appl. Energy* **2020**, *268*, 114972. [CrossRef]
32. Li, W.; León Quiroga, V.; Crompton, K.R.; Ostanek, J.K. High Resolution 3-D Simulations of Venting in 18650 Lithium-Ion Cells. *Front. Energy Res.* **2021**, *9*, 788239. [CrossRef]
33. Fedoryshyna, Y.; Schaeffler, S.; Soellner, J.; Gillich, E.I.; Jossen, A. Quantification of venting behavior of cylindrical lithium-ion and sodium-ion batteries during thermal runaway. *J. Power Sources* **2024**, *615*, 235064. [CrossRef]
34. Gillich, E.I.; Steinhardt, M.; Fedoryshyna, Y.; Jossen, A. Mechanical Measurement Approach to Characterize Venting Behavior during Thermal Runaway of 18650 Format Lithium-Ion Batteries. *Batteries* **2024**, *10*, 142. [CrossRef]
35. Willstrand, O.; Pushp, M.; Andersson, P.; Brandell, D. Impact of different Li-ion cell test conditions on thermal runaway characteristics and gas release measurements. *J. Energy Storage* **2023**, *68*, 107785. [CrossRef]
36. Shi, C.; Wang, H.; Shen, H.; Wang, J.; Li, C.; Li, Y.; Xu, W.; Li, M. Thermal Runaway Characteristics and Gas Analysis of LiNi0.9Co0.05Mn0.05O2 Batteries. *Batteries* **2024**, *10*, 84. [CrossRef]
37. Golubkov, A.W.; Scheikl, S.; Planteu, R.; Voitic, G.; Wiltsche, H.; Stangl, C.; Fauler, G.; Thaler, A.; Hacker, V. Thermal Runaway of Commercial 18650 Li-ion Batteries with LFP and NCA Cathodes – Impact of State of Charge and Overcharge. *RSC Adv.* **2015**, *5*, 57171–57186. [CrossRef]

38. Shen, H.; Wang, H.; Li, M.; Li, C.; Zhang, Y.; Li, Y.; Yang, X.; Feng, X.; Ouyang, M. Thermal Runaway Characteristics and Gas Composition Analysis of Lithium-Ion Batteries with Different LFP and NCM Cathode Materials under Inert Atmosphere. *Electronics* **2023**, *12*, 1603. [CrossRef]
39. Mao, B.; Chen, H.; Jiang, L.; Zhao, C.; Sun, J.; Wang, Q. Refined Study on Lithium Ion Battery Combustion in Open Space and a Combustion Chamber. *Process Saf. Environ. Prot.* **2020**, *139*, 133–146. [CrossRef]
40. Kriston, A.; Adanouj, I.; Ruiz, V.; Pfrang, A. Quantification and Simulation of Thermal Decomposition Reactions of Li-ion Battery Materials by Simultaneous Thermal Analysis Coupled with Gas Analysis. *J. Power Sources* **2019**, *435*, 226774. [CrossRef]
41. MacNeil, D.D.; Dahn, J.R. Test of Reaction Kinetics Using Both Differential Scanning and Accelerating Rate Calorimetries As Applied to the Reaction of Li_xCoO_2 Non-Aqueous Electrolyte. *J. Phys. Chem. A* **2001**, *105*, 4430–4439. [CrossRef]
42. Li, J.; Zhang, Z.; Guo, X.; Yang, Y. The Studies on Structural and Thermal Properties of Delithiated LixNi1/3Co1/3Mn1/3O2 (0. *Solid State Ionics* **2006**, *177*, 1509–1516. [CrossRef]
43. Li, W.; Crompton, K.; Hacker, C.; Ostanek, J.K. Comparison of current interrupt device and vent design for 18650 format lithium-ion battery caps. *J. Energy Storage* **2020**, *32*, 101890. [CrossRef]
44. Koch, S.; Fill, A.; Birke, K.P. Comprehensive gas analysis on large scale automotive lithium-ion cells in thermal runaway. *J. Power Sources* **2018**, *398*, 106–112. [CrossRef]
45. Fang, Y.J.; Qian, J.M. Isobaric Vapor-Liquid Equilibria of Binary Mixtures Containing the Carbonate Group -OCOO-. *J. Chem. Eng. Data* **2005**, *50*, 340–343. [CrossRef]
46. Cumber, P. Predicting Outflow from High Pressure Vessels. *Process Saf. Environ. Prot.* **2001**, *79*, 13–22. [CrossRef]
47. Finegan, D.P.; Scheel, M.; Robinson, J.B.; Tjaden, B.; Hunt, I.; Mason, T.J.; Millichamp, J.; Di Michiel, M.; Offer, G.J.; Hinds, G.; et al. In-operando high-speed tomography of lithium-ion batteries during thermal runaway. *Nat. Commun.* **2015**, *6*, 6924. [CrossRef]
48. Kirchev, A.; Guillet, N.; Brun-Buisson, D.; Gau, V. Li-Ion Cell Safety Monitoring Using Mechanical Parameters: Part I. Normal Battery Operation. *J. Electrochem. Soc.* **2022**, *169*, 010515. [CrossRef]
49. Fill, A.; Kopp, M.; Hemmerling, J.; Baazouzi, S.; Tendera, L.; Birke, K.P. Three-Dimensional Model of a Cylindrical Lithium-Ion Cell—Influence of Cell Design on State Imbalances and Fast-Charging Capability. In Proceedings of the 2023 IEEE 32nd International Symposium on Industrial Electronics (ISIE), Helsinki, Finland, 19–21 June 2023; pp. 1–8. [CrossRef]
50. Heenan, T.M.M.; Jnawali, A.; Kok, M.D.R.; Tranter, T.G.; Tan, C.; Dimitrijevic, A.; Jervis, R.; Brett, D.J.L.; Shearing, P.R. An Advanced Microstructural and Electrochemical Datasheet on 18650 Li-Ion Batteries with Nickel-Rich NMC811 Cathodes and Graphite-Silicon Anodes. *J. Electrochem. Soc.* **2020**, *167*, 140530. [CrossRef]
51. Lebedeva, N.P.; Persio, F.D.; Kosmidou, T.; Dams, D.; Pfrang, A.; Kersys, A.; Boon-Brett, L. Amount of Free Liquid Electrolyte in Commercial Large Format Prismatic Li-Ion Battery Cells. *J. Electrochem. Soc.* **2019**, *166*, A779–A786. [CrossRef]
52. Wang, Q.; Sun, J.; Yao, X.; Chen, C. Thermal Behavior of Lithiated Graphite with Electrolyte in Lithium-Ion Batteries. *J. Electrochem. Soc.* **2006**, *153*, A329. [CrossRef]
53. Steinhardt, M.; Gillich, E.I.; Rheinfeld, A.; Kraft, L.; Spielbauer, M.; Bohlen, O.; Jossen, A. Low-Effort Determination of Heat Capacity and Thermal Conductivity for Cylindrical 18650 and 21700 Lithium-Ion Cells. *J. Energy Storage* **2021**, *42*, 103065. [CrossRef]

Disclaimer/Publisher's Note: The statements, opinions and data contained in all publications are solely those of the individual author(s) and contributor(s) and not of MDPI and/or the editor(s). MDPI and/or the editor(s) disclaim responsibility for any injury to people or property resulting from any ideas, methods, instructions or products referred to in the content.